Chapter 4

INTERACTIONS OF HIGHLY CHARGED IONS WITH C_{60} AND SURFACES

U. Thumm
J. R. Macdonald Laboratory, Department of Physics, Kansas State University
Manhattan, Kansas 66506–2604, USA
Uwe.Thumm@phys.ksu.edu

Abstract Slow collisions between highly charged ions and many-electron targets, such as large atoms, molecules, clusters, or surfaces, usually lead to the transfer of several electrons from the complex target to the projectile. The efficient capture of target electrons is related to the relatively long (on an atomic time scale) interaction time of typically several femtoseconds and the strong Coulomb force of the highly charged projectile that acts like a vacuum cleaner for loosely bound target electrons while offering a large number of excited projectile states into which electrons can be captured. This chapter will cover part of the interesting physics involved in collisions with two particular types of complex targets: gaseous C_{60} (as a representative for easily mass-selected carbon-cage molecules called "fullerenes") and solid surfaces. The theoretical description of these collisions is presented as simply as possible, with a strong emphasis on the modeling of basic electronic interaction mechanisms. For C_{60} targets, a variety of observables recently have been measured in laboratories around the world against which existing models can be scrutinized. While for C_{60} targets modern coincidence experiments allow for the selection of distant projectile trajectories that do not result in the destruction of the target's carbon cage, even in the most grazing collisions between highly charged ions and surfaces, close encounters cannot be avoided. This complicates the study of collisions with surfaces to the extent that the interaction mechanisms which dominate while the ion is close to (and possibly inside) a surface are not yet understood in full detail. These mechanisms are a matter of intense ongoing research to which the reader will be introduced in this chapter.

Keywords: solid surfaces, fullerenes, $C_{60}, many-electrontargets, electronicinteractionmechanisms$

1. Introduction

Highly charged ions (HCIs) carry a large amount of potential energy. This energy equals the sum of successive ionization energies required to remove a given number of electrons in order to generate an ion in a particular charge state. A significant fraction or all of this energy may be released whenever an HCI gets in contact with matter and may lead to the fragmentation of a molecular or cluster target, to the creation of blisters and craters on the surface of solid targets, to the emission of a large number of electrons in collisions with complex targets, and to the "sputtering" of atoms and ions during the impact on solid surfaces. For the past few years, the high energy density of HCIs and the fact that very fast HCIs traveling through matter (e.g. water or organic tissue) deposit most of their total energy over a well localized volume have allowed for the successful treatment of certain cancers in otherwise inaccessible parts of the human body [1]. Other applications include the use of HCIs for ion lithography [2, 3], which is of particular interest to the semiconductor industry [4]. These technological advances are unthinkable without prior basic research in atomic, molecular, solid state, and surface physics. They serve as a motivation for the detailed investigations of HCI–matter interactions reviewed in this chapter.

The basic physical processes that occur during the interactions of HCIs with gaseous matter, i.e. atoms or molecules, have been studied in great detail for over two decades. A comprehensive body of work, both experimental and theoretical, exists for a large variety of projectile ions, targets, and kinetic energies of the incident projectile. Next to spectroscopy, atomic collisions constitute one of the pillars on which our understanding of atoms and molecules rests. The basic collision processes investigated for gaseous atoms and molecules are usually classified by the elementary electronic processes of interest. For atomic targets, these are excitation and ionization processes of either collision partner and combinations thereof, e.g., the simultaneous transfer of one electron from one collision partner to the other accompanied by electronic excitation (so–called "transfer excitation"). For molecular targets, collision processes become more complex as the relative nuclear motion within the molecules gets affected by the collision. This may result in collisionally induced vibrational and rotational excitation or fragmentation of the molecule.

Clusters are large molecules and, therefore, all mechanisms that are operative in interactions between ions and simple molecules also will appear in collisions with clusters, complicated by their larger number of constituents (electrons and nuclei). For example, while the simplest molecule (H_2) can fall apart only into a few fragment combinations (H+H, p+H, p+p), a C_{60} fullerene might undergo multiple fragmentation into vibrationally excited fragments, which subsequently split into smaller fragments and yield a wide distribution of fragment masses.

With respect to increasing complexity of the target, ion–cluster collisions fall intermediate between ion–atom and ion–surface interactions. Cluster targets, C_{60} in particular, combine many features of charge transfer from atoms in the gas phase and from surfaces. In the early nineties, gaseous C_{60} became a popular target for collision experiments with ions owing to the convenience with which it is handled in the laboratory. While metal clusters are usually generated with a broad mass (size) distribution, C_{60} is available in pure form in macroscopic amounts as a target of specific mass (720 amu). This eliminates the need of either mass–selecting charged target clusters before the collisions take place (at the expense of reducing the target density and count rate in the experiment) or, alternatively, of carrying out experiments in which detailed information gets lost due to the inherent averaging over cluster masses. The truncated icosahedral molecular structure and its large number of vibrational degrees of freedom make the highly symmetrical C_{60} cluster unusually stable [5]. Due to the large number of vibrational degrees of freedom, a perturbation to the cage structure of the cluster can quickly equilibrate over the cluster. This tends to avoid the accumulation of enough vibrational energy over the volume of individual chemical bonds to induce fragmentation by breaking carbon–carbon bonds. Thus, due to its relatively large thermal stability, C_{60} can be evaporated easily and serve as a gaseous target for incoming electrons [6, 7], ions [5, 8], and charged clusters [9]. The cage-structure of C_{60} was observed to withstand the reflection from a surface [10], and photoionization and collision experiments with HCIs have produced C_{60}^{i+} ions in positive charge states up to i=9 [11] that do not dissociate ("Coulomb explode") for at least several microseconds.

Highly charged projectile ions are particularly suitable for investigations of the dynamic electronic response of C_{60} clusters to a strong external perturbation that may significantly distort the electronic charge distribution of the easily polarizable target and lead to the capture and emission of a large number of electrons. In this context, “dynamic” means that the cluster–electron distribution continuously adjusts itself to the Coulomb force of the moving projectile. In recent coincidence experiments the deflection of slow Ar^{8+} projectiles was found to depend sensitively on the dynamic polarizability of the target [12]. The analyses and theoretical modeling of such collisions provide not only an important tool for examining properties of fullerenes and their basic interaction mechanisms with highly charged projectile ions, but also allow for the study of the complicated electronic dynamics involved in the collisional creation and post-collisional decay of unstable and multiply excited projectiles (hollow ions) due to Auger electron and X-ray emission[11, 13–15]. So–called “Auger electrons” are emitted in relaxation steps that involve two active projectile electrons.

Within a simplified picture of this Auger transition, one active electron transits to a lower electronic projectile shell while transferring the energy released in this transition to the second active electron that is emitted. In contrast, the emission of X rays requires only one active electron. This simplified explanation in terms of one active electron neglects collective electron readjustments ("configuration interactions") that happen in ions with at least two electrons in response to the primary radiative transition Interactions with ions contribute to our understanding of the electronic response of delocalized fullerene electrons in the initial phase of a chemical reaction that leads to the binding of reactive groups. In this way, the study of fullerene interactions with ions may contribute to the analysis of reactions in the new field of fullerene chemistry. More complex than aromatic chemistry, which is based on the two–dimensional ring structure of benzene, fullerene chemistry is based on three–dimensional carbon–cage molecules and may allow for the synthesis of new chemicals and pharmaceuticals of unforeseen properties and efficiency.

The emerging field of slow HCI–C_{60} interaction studies was significantly stimulated by experiments conducted at Kansas State University and at the University of Giessen [16]. In rapid succession, fullerenes were used in atomic collision laboratories around the world in the nineties. These experiments first probed the interaction between slow, highly charged ions and gaseous C_{60} targets by measuring the final charge–states of target and projectile in coincidence. One of the striking features of these coincidence measurements is the distinction between hard collisions and non–destructive, soft collisions. Hard collisions occur at relatively small impact parameters and lead to fragmentation of the target–carbon cage. In contrast, soft collisions occur at relatively large impact parameters (always larger than the C_{60} radius), can result in the capture of several electrons, and do not lead to the immediate fragmentation of the target. To some extent, in soft, more distant collisions, a fullerene may be viewed as a spherically bent monolayer of a graphite surface. Details of the target electron distribution are less important for the interaction with a distant projectile. Soft HCI—C_{60} collisions allow for the investigation of "above surface" effects, which are disguised by the more violent interaction dynamics in hard collisions with C_{60} and for small ion–surface distances in surface collisions [17]. Very recently, triple coincidence measurements have been performed [15] in which the ejected number of electrons is detected along with the final charge state of the projectile and with the mass and charge of the recoiling target or target fragments. These experiments resolve the many–electron interaction dynamics in unprecedented detail and allow, for example, the discrimination between the number of electrons captured into excited projectile states and the number of "stabilized" projectile electrons that are kept after the projectile has relaxed into its ground state.

Collisions of HCIs with metal surfaces have been a subject of intense experimental and theoretical interest for more than a decade, and several characteristics of the electron exchange and emission processes are becoming well established [17–32]. In contrast to soft collisions with buckyballs (C_{60}), collisions with surfaces always involve close encounters with target atoms. The attractive interaction between the positively charged projectile and the negative image charge it induces in the surface bends the projectile trajectory towards the surface, even at the most grazing angles of incidence, and leads to a large overlap of target and projectile electronic states.

Insulator surfaces have been added to the list of target materials more recently, and interesting new phenomena are being investigated [33–38]. Recent experiments have measured the final charge state distribution of the surface–scattered projectile [19, 30, 32], the projectile deflection angle [33, 39], and the emission of electrons [17, 25, 26, 29, 34, 40] and photons [18, 23, 24, 37] during and after the projectile–surface interaction.

The remainder of this chapter is organized in the following way. Section 4.2 reviews resonant electron exchange and the emission of projectile Auger electrons during and after soft collisions of an HCI with C_{60}. In section 4.2.1, we give an overview of the dynamical classical over–barrier model (COM). Section 4.2.2 illustrates the dynamic shift of projectile and target energy levels during the interaction. Section 4.2.3 includes remarks on the electronic structure of C_{60}. Numerical results for charge–state evolutions and emitted electron yields follow in section 4.2.4. In the subsequent subsections, theoretical predictions of the dynamical COM are discussed and compared with recently measured observables, such as cross sections for the capture of a specific number of target electrons (section 4.2.5), final projectile charge states (section 4.2.6), the projectile kinetic image energy gain (section 4.2.7), and the projectile scattering angle (section 4.2.8).

Collisions with surfaces are reviewed in section 4.3. In section 4.3.1, we discuss the forces that determine the motion and kinetic energy change of the projectile ion along its classical path. In section 4.3.2 we describe the basic elements in the modeling of HCI–surface collisions by extending the COM of section 4.3.1 in order to include interactions that become dominant close to (and inside) the target surface. Section 4.3.3 summarizes these interaction mechanisms in the form of a set of rate equations for the occupation numbers of projectile shells. In section 4.3.4 simulations done within the extended COM are compared with measured final charge–state distributions of reflected ions and emitted electron yields. A brief summary follows in section 4.4. Unless otherwise stated, atomic units are used throughout this chapter. In these units, the elementary charge, the electron mass, Planck's constant divided by 2π, and the Bohr radius are equal to one ($e = m = \hbar = a_0 = 1$).

2. Collisions of Highly Charged Ions with C_{60}

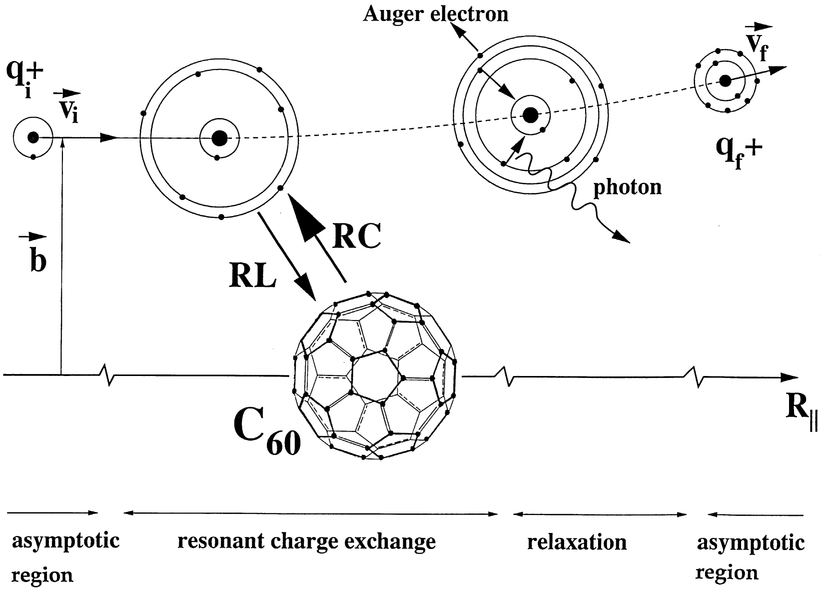

Figure 4.1. Sketch of the collisions scenario (not to scale). A highly charged ion with initial charge q_i, velocity $\vec{v}_i$, and impact parameter $\vec{b}$ carries one tightly bound electron into the collision. At distances of the order of 10 to 100 a.u. from the target center it resonantly captures (RC) and (to a lesser extent) loses (RL) electrons. This leads to a positively charged target and a multiply excited, hollow projectile. Downstream and past the resonant interaction region, the unstable hollow projectile relaxes by emitting Auger electrons and X-ray photons. It may then be detected with final charge state q_f and velocity $\vec{v}_f$. The projection of the target–projectile distance R onto the incident–beam direction is denoted by $R_{||}$.

The basic scenario for a distant collision between an HCI and a C_{60} cluster is sketched in fig. 4.1. On an incident trajectory that is determined by the impact parameter $\vec{b}$ and the asymptotic velocity $\vec{v}$ of the incident projectile, starting at a distance of typically ten to 50 atomic units from the target center, an HCI captures resonantly several electrons into excited states. The distance at which the capture sequence starts primarily depends on the charge state of the incident ion and the ionization energy of the cluster. "Resonant" capture means that the active electron is transferred to a projectile electronic state that has about the same energy as its original target electronic state. The capture sequence typically ends shortly after the projectile has passed the point of closest approach to the fullerene target and results in the formation of a multiply excited ("hollow") ion. These collisionally formed hollow ions are electronically unstable

Table 4.1. Time scales relevant for the formation and relaxation of hollow ions (of core charge q_{core}). Typical values for 80 keV Ar^{8+} interacting with C_{60}. The plasmon response time is estimated as $\sqrt{\frac{2\pi}{n_{el}}}$, where n_{el} is the average electron density of C_{60}.

collision time for resonant exchange:	5 fs
orbiting time of first active projectile level (n=7):	0.8 fs
plasmon response time of C_{60}:	0.2 fs
average time between successive electron capture events:	0.3 fs
projectile Auger transitions:	> 0.1 fs
projectile radiative transitions:	$q_{core}^{-4} \cdot 10^{-8}$ s

and release their excitation energy by emitting electrons and photons. Compared to the time it takes to form the hollow ion by multiple electron capture (typically a few femtoseconds) , some relaxation steps are slow, and the full relaxation of the excited projectile can be completed only during a relatively long time, downstream from the target. In typical experiments, the time of flight of the projectile between the interaction region and the detector is of the order of microseconds and long enough to allow for complete relaxation. Relevant time scales for a typical collision system are assembled in table 4.1.

2.1 The formation of hollow ions in ion–C_{60} collisions

The main aspects of the interaction between slow highly charged ions and complex atomic or molecular targets can be described by using mostly classical model assumptions. In COMs the electronic interaction with highly charged ions is modeled within the independent electron picture and is based on the effective potential to which an active electron, i.e. an electron that might be captured or lost, is subjected. An important feature of this effective potential is the potential barrier located between target and projectile. Position and height of the barrier change during the collision due to the relative motion and changing electronic structure of the collision partners. The COM allows for resonant transitions if the motion of a target or projectile electron across the potential barrier is classically possible, if the initial electronic state is at least partly occupied, and if the final state is not fully occupied in order to prevent Pauli blocking, i.e., the violation of Pauli's exclusion principle that excludes two electrons from occupying the same quantum state. The basic idea of classical capture over a potential barrier is show in fig. 4.2. In the past, various versions of over–barrier models have been applied successfully to slow collisions of ions with atoms [41–43], surfaces [21, 38], and clusters[12, 14, 16, 27, 44, 45]. The model of Bárány and Setterlind [27] represents C_{60} as a dielectric sphere. Radius a and dielectric constant ϵ of the sphere are free parameters.

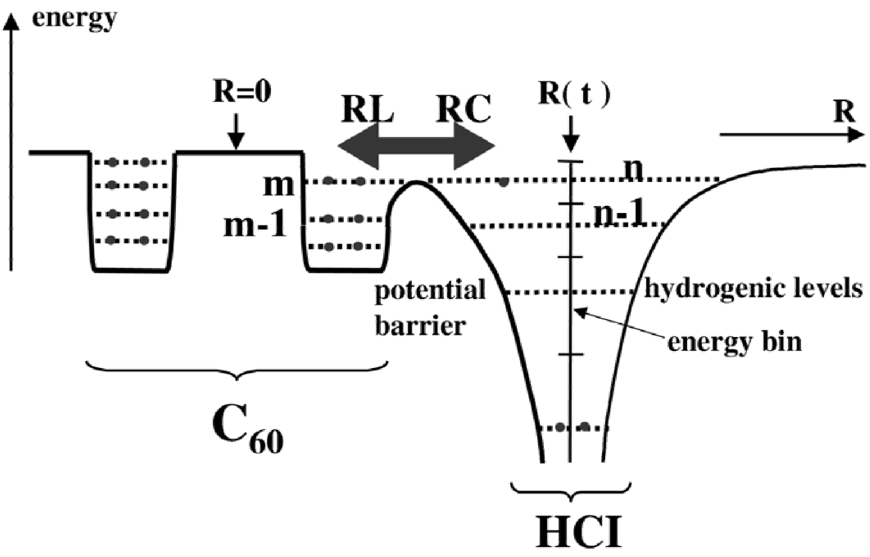

Figure 4.2. Basic idea of the classical over–barrier model applied in this chapter. The effective potential governs the motion of an active electron between the C_{60} target (centered at $R = 0$) and a highly charged ion (HCI) at a distance $R(t)$. Resonant capture (RC) and resonant loss (RL) of electrons occur across the potential barrier

For applications to collisions of slow Ar^{8+} with C_{60}, this model agrees well with experiments and other theories [16, 44]. An attractive feature in all COMs is that basic ideas of classical dynamics and electrostatics yield reasonable estimates for charge–transfer cross sections, charge–state distributions, and other observables, the computation of which is beyond the technical feasibility of full quantum calculations. Details of the best specific formulation of the model remain under investigation. For very slow projectiles, ionization of the target occurs slowly with a small transfer of electronic energy, leaving the C_{60} vibrationally and electronically cold with a high probability of surviving the ionization intact. In the experiment of Walch *et al.* [16] it was shown that C_{60}^{i+} up to i=6 could be produced in this manner with slow Ar^{8+} ions incident on C_{60} with relevant impact parameters in the range of typically 10 to 30 a.u.. Jin *et al.* [11] used a more highly charged projectile, Bi^{44+}, to produce C_{60}^{9+}. For charge states $i < 9$, Jin *et al.* found C_{60}^{i+} ions with lifetimes of at least 5μsec.

During the ion–cluster interaction, energy levels, level occupations, transition rates, and total charges of target and projectile change as a function of R, the distance between the centers–of–mass of target and projectile. For the slow collisions considered in this chapter, R does not change on the time scale of resonant electronic transitions, and an adiabatic approximation is generally justified. In order to be captured or recaptured, the active electron is required to overcome the potential barrier V_B between target and projectile that is formed by the total electronic potential

$$V(q_p, q_t, R, z) = -\frac{q_p}{|R-z|} - \frac{q_t}{z} + V_{im}(q_p, R, z) \tag{4.1}$$

where q_p and q_t are the charges of projectile and target acting on the electron in transition. The electron coordinate along the "inter-nuclear axis" is denoted by z. This axis joins the C_{60} center and the projectile nucleus with the origin at the buckyball center of mass. The image potential, V_{im}, includes the active electron's interaction with its own image charge and with the image of the effective projectile charge q_p in the target. The barrier height V_B is found numerically for any distance R as the maximum of $V(q_p, q_t, R, z)$, considered to be a function of z.

As the projectile approaches the target, the first resonant capture (RC) of an electron becomes possible at the distance R_1^* between the projectile and target centers–of–mass, when V_B energetically moves below the highest occupied target level. Similarly, as R decreases, a second, third, etc. electron may be captured at critical distances $R_2^* > R_3^* \ldots$ on the incoming trajectory. Note that for the purpose of investigating electron capture mechanisms, the heavy projectile may be assumed to move along a straight–line trajectory (projectile scattering angles in typical experiments are of the order of a few mrad, cf. section 4.2.8 below). The critical distances R_i^* are then equal to critical impact parameters at which the trajectory becomes tangent to a sphere of radius R_i^* about the target center. Since the *dynamical* COM discussed in this chapter treats the electronic charge as a continuous parameter, some assumption has to be made as to when a complete elementary charge has been transferred. This leaves some freedom in the precise definition of critical radii. We define R_1^* as the impact parameter at which charge begins to flow from the target to the projectile and R_2^* as the impact parameter at which one unit of charge has left the target, etc.

The projectile may be described within an independent electron approach, based on hydrogenic shells n with energy levels, occupation numbers, and degeneracies denoted by $\epsilon_n^p(R)$, $a_n(R)$, and $A_n = 2n^2$, respectively. Angular momentum sub-levels are not resolved. The time evolution of the occupations $a_n(t)$ and $b_m(t)$ of projectile shells n and target levels m are obtained by integrating classical rate equations of the form

$$\begin{aligned} \frac{d}{dt}a_n &= \Theta(A_n - a_n)\Gamma_n^{RN} - \Gamma_n^{RL}\, a_n + \sum_{n'>n}\Gamma_{n',n}^{AI} - 2\sum_{n'<n}\Gamma_{n,n'}^{AI} \quad (4.2) \\ \frac{d}{dt}b_m &= \Gamma_n^{RL}\, a_n - \Gamma_n^{RN}, \quad (4.3) \end{aligned}$$

with the known initial occupations of projectile and target, a_n^0 and b_m^0. Θ is the unit step function. Analytical expressions for the RC rates Γ_n^{RN} and RL rates Γ_n^{RL} can be derived as classical transfer currents [44, 46]. Resonant transition rates and occupation numbers depend on $R(t)$, and the above equations are solved numerically, together with Newton's equation for the projectile motion. In particular, the resonant neutralization rate Γ_n^{RN} depends on the populations b_m of all (energetically shifted) target levels m that lie within a small interval around the (shifted) energy of the resonant projectile level n. Within the dynamical COM this "energy binning" is necessary in order to relate classical transfer currents to discrete quantum levels [44, 46]. Simplified illustrations of the elementary electronic processes in eqs. (4.2) and (4.3) are given in fig. 4.3.

For the two last terms in eq. (4.2), it is sufficient to include only fast Auger transitions for which the two active electrons start in the same shell and which may, to a small extent, deexcite a multiply excited projectile while competing resonant electron transfer occurs. An analytical approximation to these fast Auger rates,

$$\tilde{\Gamma}^{AI}_{n_{\text{ini}},n_{\text{fin}}} = \frac{5.06 \cdot 10^{-3}}{(n_{\text{ini}} - n_{\text{fin}})^{3.46}}\,, \tag{4.4}$$

was obtained by Burgdörfer *et al.* [20] by fitting atomic structure calculations [20, 47]. In addition to $\tilde{\Gamma}^{AI}_{n_{\text{ini}},n_{\text{fin}}}$ in eq. (4.4), the Auger transition rates $\Gamma^{AI}_{n_1,n_2}$ in eq. (4.2) include statistical weights. These empirical statistical factors, $1/(1+1.5a_n)$ and $\frac{1}{2}a_n(a_n-1)$, correct for the decrease of Auger transition rates for increasing populations a_n of the final shell and take the equivalence of electrons in the initial shell into account, respectively [44, 48]. Slow Auger relaxation channels are not included in eq. (4.2) because they can be neglected *during* the collision (cf. table 4.1). Further downstream, however, when resonant transfer processes are classically forbidden, slow Auger processes become crucial in determining the final charge–state of the projectile. Downstream Auger and radiative relaxation steps determine the observable final charge state of the projectile and can be accounted for by enhancing the dynamical COM with a post–collisional relaxation scheme [14] (see section 4.2.6 below).

2.2 The shift of target and projectile electric levels during the collisions of highly charged ions with C_{60}

During the collision, projectile energy levels shift due to image–charge effects, Stark shifts induced by a charged target, and the dynamical change in screening induced by varying level populations. Target energy levels $\epsilon^t_m(R)$ are shifted downward in the strong attractive electric field of the positive projectile. After the capture of target electrons, positive charge accumulates on the target, which results in an additional downward shift of the target and projectile spectra.

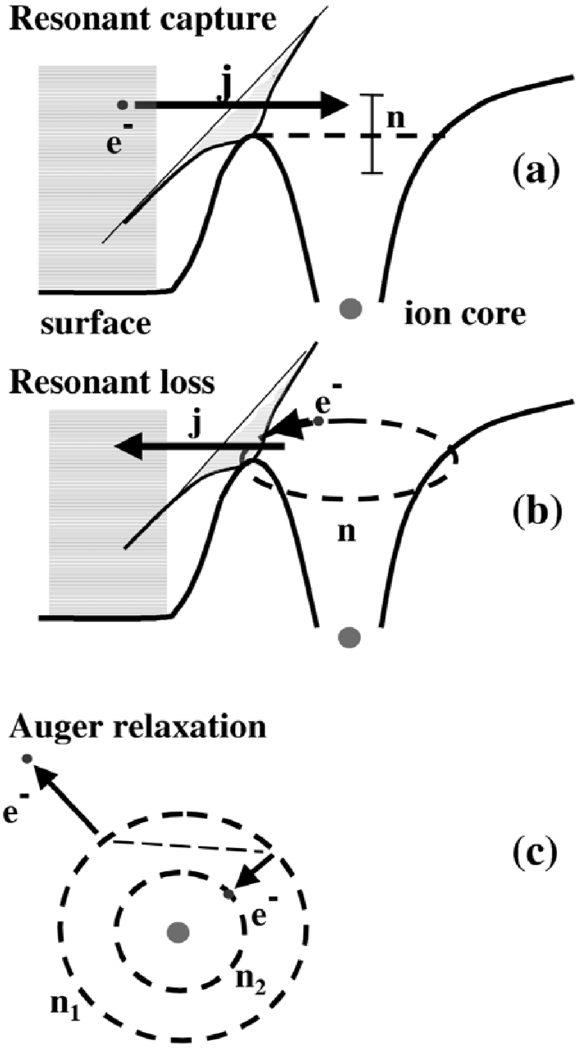

Figure 4.3. Illustration of resonant capture by (a) and resonant loss from (b) a highly charged ion, modeled as a classical current across a potential barrier. The Auger process (c) involves two electrons, one of which is emitted.

In order to understand how the occupation of target and projectile levels changes in response to resonant electron transfer processes, it is instructive to look at the energies of target and projectile levels relative to the top of the potential barrier as a function of $R_{||}$. With $R_{||}$ we denote the projection of the distance between the target center–of–mass and the projectile onto the incident

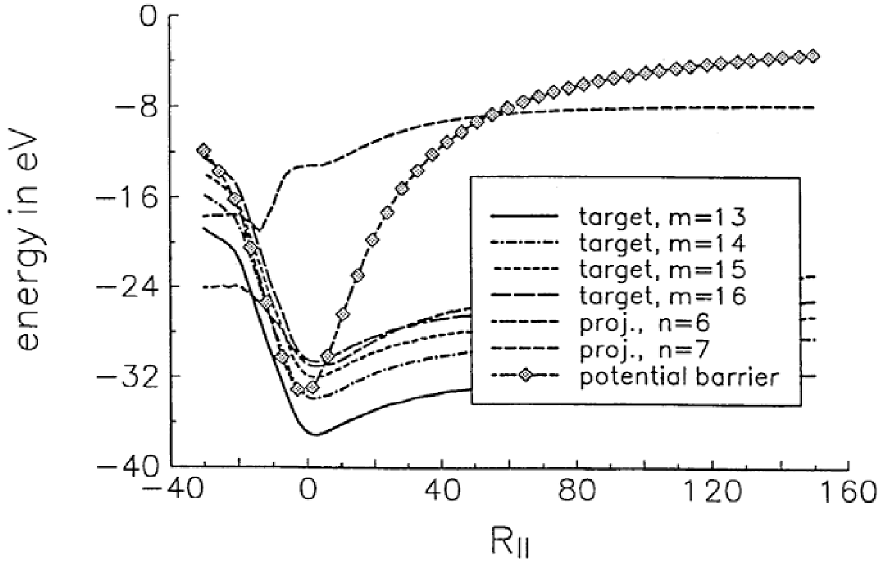

Figure 4.4. Shift of target and projectile energy levels relative to the potential barrier for classical over–barrier capture as a function of the distance $R_{||}$ for 80 keV Ar^{8+} ions colliding with C_{60}.

beam direction (cf. fig. 4.1). For 80 keV (corresponding to a speed v=0.28) Ar^{8+} ions colliding with C_{60} with impact parameter $b = 15$, fig. 4.4 shows that projectile level $n = 6$ crosses the highest occupied target level (the Fermi level), labeled '$m = 15$'. The crossing happens above the potential barrier and near the point of closest approach. This results in a large current of target electrons from level $m = 15$ that are classically allowed to transfer to projectile level $n = 6$. Similarly, projectile level $n = 7$ crosses the same target level on the incident trajectory and above the barrier. The corresponding rapid resonant filling of projectile levels $n = 6$ and $n = 7$ is seen in fig. 4.5a (see section 4.2.4, below).

2.3 On the electronic structure of C_{60}

Large metallic clusters and C_{60} have band structures similar to metal surfaces with regard to a large portion of unoccupied states above the Fermi level. Smaller clusters tend to form narrowly spaced levels, rather than bands and, with respect to capture, may resemble a large atomic target.

The ground–state electronic structure of neutral C_{60} is well understood from first–principles calculations [46, 49–52]. In the calculation underlying fig. 4.4, the asymptotic energies of the target levels were taken from the local density

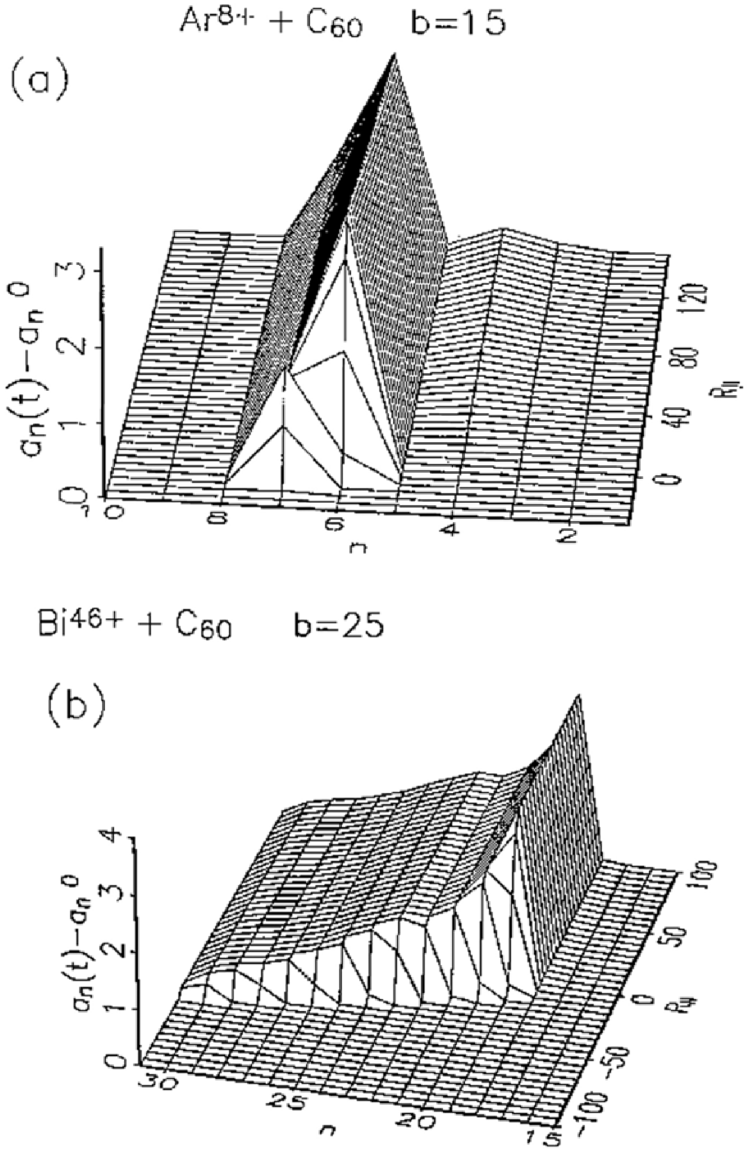

Figure 4.5. Evolution of projectile level occupations in collisions with C_{60}. The point of closest approach is at $R_{||} = 0$. (a) For incident 80 keV Ar^{8+} projectiles and impact parameter $b = 15$. The graph shows the dynamical change $a_n(t) - a_n^0$ in the population of projectile shells $n = 1$ to $n = 10$. The initial shell population is denoted as a_n^0. $a_n(t)$ is the population of shell n at the distance $R_{||}(t)$. (b) For 830 keV Bi^{46+} and $b = 25$.

functional approximation (LDA) calculation of Puska and Nieminen [49] in which the occupied valence states of C_{60} are represented by 15 highly degenerate levels. In all other applications to charge exchange and electron emission in soft ion–C_{60} collisions discussed in this chapter, multi–center self–consistent Dirac–Fock–Slater (DFS) calculations [46, 52] were employed to obtain the ground–state electronic structures of neutral C_{60} and its positive ions $C_{60}^{i+}, i = 0...6$. These calculations assumed that the cage structure does not change with the charge state i. The charge–state independent buckyball radius was taken as $a = 6.7$ [49, 50]. The calculations yield DFS single particle energies of C_{60}^{+i} for $i = 0 \ldots 7$ and the sequence of ionization potentials $I_{i=1...7} = 7.24, 10.63, 14.01, 17.44, 20.78, 24.24$, and $27.54\ eV$, in good agreement with other calculated [46, 49–52] and experimental data [6, 53, 54].

In agreement with the simple electrostatical picture that represents the charged C_{60} cluster as a uniformly charged sphere, the incremental increase of ionization energies is due only to the net charge of the cluster. Therefore, the sequence of ionization potentials increases linearly with the net cluster charge. Thus, higher, not reliably measured or exactly calculated ionization potentials $I_i,\ i > 7$ can be approximated by taking into account the work necessary to remove an eighth, etc., electron from the surface of a conducting sphere, $I_i = I_1 + (i-1)/a$ [44].

The LDA calculation of Puska and Nieminen [49] and the DFS calculation show noticeable differences in the calculated valence spectra of neutral C_{60}. However, the comparison of scattering calculations, based on the two different descriptions of the target–electronic structure [46], shows that cross sections for the production of specific target–charge states in soft collisions and charge–state evolutions of target and projectile agree within 10 per cent. This relative insensitivity of total capture cross sections to details of the C_{60} electronic structure is consistent with the primary importance of the sequence of target ionization energies I_i and the matching of (shifted) energy levels of target and projectile, as illustrated in section 4.2.2.

2.4 Charge–state evolution and electron emission during the collision

fig. 4.6 shows typical charge–state evolutions in HCI–C_{60} interactions, as a function of $R_{||}$. The changes are equal to the difference of the instantaneous occupation and the initial occupation of a particular projectile shell. The figure shows results for incident Ar^{8+} at a kinetic energy of 80 keV on a trajectory with impact parameter $b = 15$ (fig. 4.5a) and Bi^{46+} at 830 keV with $b = 25$ (fig. 4.5b). For the Ar^{8+} projectile, the $n = 6$ and $n = 7$ shells get resonantly populated on the incoming trajectory (cf. fig. 4.4 in section 4.2.2). This agrees with experimental evidence for capture into the $n = 7$ shell [16, 55]. Auger relaxation of the projectile on the outgoing trajectory ($R_{||} > 0$) leads to the

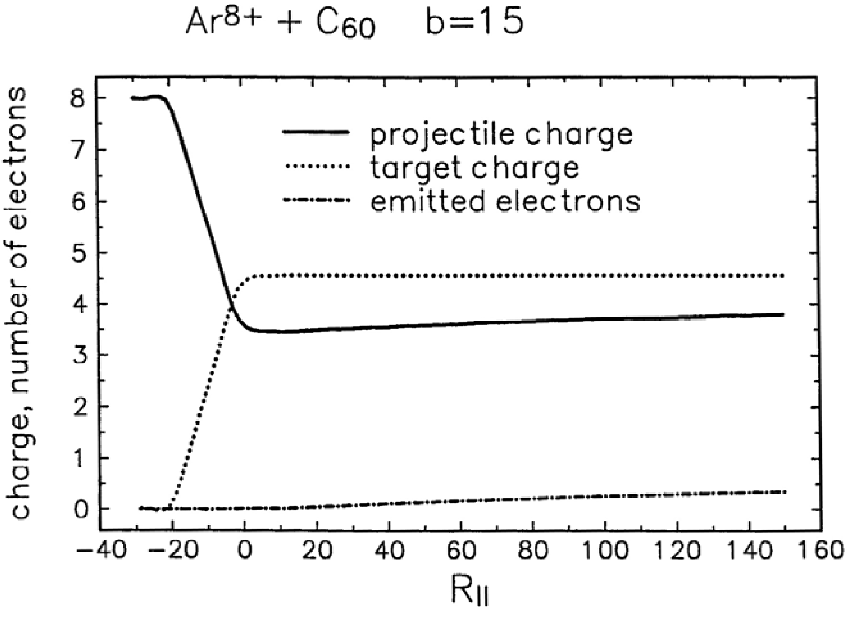

Figure 4.6. Projectile and target charge–state evolution and accumulated projectile Auger emission for incident 80 keV Ar^{8+} projectiles colliding with C_{60} at impact parameter $b = 15$.

partial depletion of projectile shells $n = 6$ and 7 and increases the population in projectile levels with $n = 3$ and $n = 4$.

The degree of population inversion achieved with incident Bi^{46+} projectiles is rather spectacular. Fig. 4.5b shows that resonant transitions first populate projectile shell $n = 31$ and, as the projectile further approaches the target, eventually lead to the population of projectile shells with principal quantum numbers between 19 and 31. The dynamical COM predicts that the large current of resonantly captured electrons originates in nearly degenerate levels near the Fermi level of C_{60} [14].

The charge–state evolutions in fig. 4.6 follow directly from the time–dependent occupations in eqs. (4.2) and (4.3). The projectile continues to relax by emitting electrons as it moves further away from the target and after charge exchange has become impossible (see section 4.2.6 below). However, in the average, Auger transitions are too slow to significantly depopulate excited projectile levels within the short collision time interval of about 15 fs covered in figs. 4.5a and 4.6. Therefore, the accumulated current of emitted Auger electrons displayed in fig. 4.6 and the increase of the net projectile charge on the part of the outgoing trajectory shown in the figure are very small.

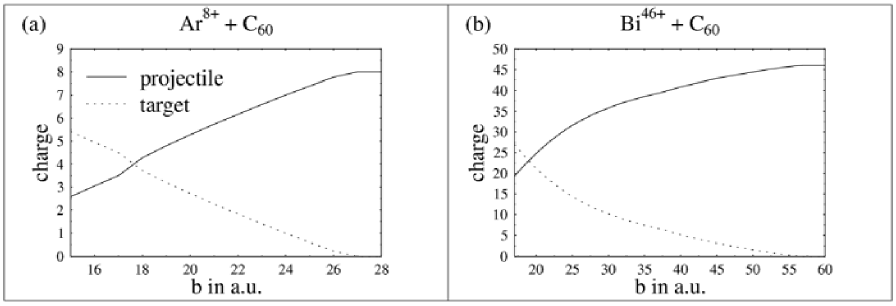

Figure 4.7. Projectile and target charge states as a function of the impact parameter b immediately after resonant electron exchange has ceased at $R_{||} = 150$. (a) For incident 80 keV Ar^{8+} projectiles. (b) For 830 keV Bi^{46+}.

The charge states of target and projectile as a function of the impact parameter and at a distance $R_{||} = 150$ on the outgoing trajectory are shown in fig. 4.7. At this distance all resonant electron transfer has stopped. The comparatively slow projectile Auger transitions had no time to relax the projectile. A lower limit for the impact–parameter range of non–destructive collisions is given by the highest charge state the target ions support without falling apart while interacting with the projectile. At the smallest impact parameter $b = 15$ in fig. 4.7a, the incident Ar^{8+} ion captures five electrons and thus maintains the carbon cage of the target [16]. At the smallest impact parameter in fig. 4.7b, the incident Bi^{46+} has captured a large number of electrons, which eventually leads to fragmentation of the target. In this case, the dynamical COM is applicable under the realistic assumption that the multiply charged fullerene is stable *during* the collision, i.e. at least for several femtoseconds.

2.5 Cross–sections for multiple electron capture

Similar to a solid surface, C$_{60}$ provides a large reservoir of electrons with nearly the same binding energies and thus the cross section for the transfer of many electrons falls slowly with the number of electrons captured. With regard to an insulating target surface or an atomic target, electron capture by an HCI results in a multiply charged target. Figs. 4.5 and 4.6 illustrate the capture of several electrons by an HCI on its incident trajectory. The sequence of critical radii R_i^* for the capture of i electrons can be extracted from the impact parameter dependence of the final target charge state shown in fig. 4.7. The critical distances R_i^* for sequential over–barrier capture are related to geometrical cross sections for the production of specific charge states, $+i$, of

C_{60} by

$$\sigma_i = \pi({R_i^*}^2 - {R_{i+1}^*}^2) \tag{4.5}$$

and to the total geometrical cross section for charge exchange in non–destructive collisions by $\sigma_{tot} = \pi {R_1^*}^2$. This method for the calculation of cross sections has been applied to 50 keV N^{5+} [45], $3.3q$ keV Ar^{q+}, $q = 8, 15$ [56], and 830 keV Bi^{46+} [14] colliding with C_{60}.

(a) Critical radii for C_{60}^{i+} production

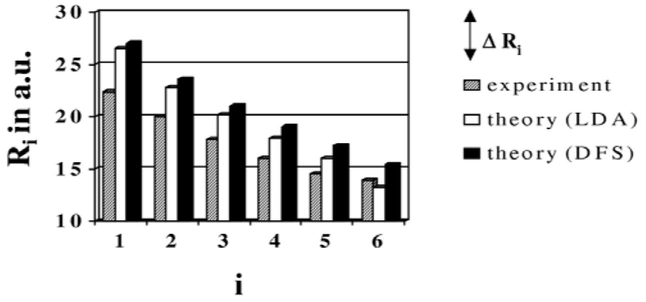

(b) Cross sections for C_{60}^{i+} production

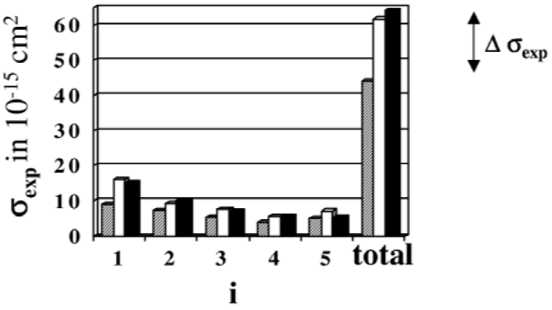

Figure 4.8. Critical radii R_i for sequential over–barrier capture (a) and corresponding cross sections (b) for capture of one to five electrons in collisions of 80 keV Ar^{8+} with C_{60}. Experimental results in comparison with simulations based on both LDA and DFS calculations of the C_{60} electronic structure.

Fig. 4.8 shows results for the system 80 keV Ar^{8+} on C_{60} discussed earlier in this chapter (cf. figs. 4.4, 4.5a, 4.6). The cross sections in fig. 4.8b are based on the critical radii in fig. 4.8a. The double arrows indicate experimental errors, ΔR and $\Delta\sigma_{exp}$, for critical radii and cross sections. Theoretical results are depicted in fig. 4.8 for simulations based on both, LDA [49] and DFS [46] calculations for the electronic structure of C_{60}. The calculated COM total cross sections agree with the absolute measurements for incident Argon ions performed by Walch *et al.* [16, 44] and by Selberg *et al.* [55, 56].

2.6 On the relaxation of hollow ions

In contrast to HCI–surface collisions, for cluster targets the hollow ion formed in the sequence of capture processes is not necessarily destroyed, but is likely to survive and deexcite far downstream. This offers the possibility of examining the complicated relaxation dynamics of multiply excited ions on the exit trajectory and at large distances where electron capture has ceased. Collisions with clusters are similar to the ion-atom case in that an intact recoil ion often remains whose charge state can be used to determine the number of electrons initially removed from the target.

Hollow ions, created in ion–cluster collisions, decay during the typically several microseconds of flight time the projectile needs to cover the macroscopic distance between the collision (resonant–exchange) region and the detector (cf. fig. 4.1 and table 4.1). This downstream decay can be modeled as a sequence of auto–ionizing and radiative relaxation steps [14]. Typically the HCI starts to relax via a cascade of Auger transitions. During these transitions lower lying levels are populated. Later, when the Auger relaxation cascade has populated lower–lying shells, radiative transitions may start to compete for subsequent relaxation steps. This is in agreement with known typical branching ratios (radiative versus non–radiative transition rates) which put increasing weight on radiative transitions as lower shells are populated. Radiative relaxation steps may then proceed along the “Yrast” line of maximal angular momentum of the active electron. This is supported by the statistical dominance of high angular momentum states, the dipole selection rule ($\Delta l = 1$), and the resonant population of high angular momentum states at large impact parameters.

Attempts to model the intricate relaxation of multiply excited ions have been made in the past. Benoit–Cattin *et al.* [57] have investigated the relaxation of doubly, triply, and quadruply excited projectile states formed in collisions of 70 keV N^{7+} ions with argon. Their discussion of possible relaxation paths is based on measured electron spectra in conjunction with predictions of the COM of Niehaus [42]. The emitted electron spectra are dominated by doubly excited lines, which are traced to excited states formed by either direct double capture or auto–ionizing cascades. Radiative stabilization following double electron capture of 10 keV/amu $Ar^{q+},\ q \leq 17$ and $Kr^{q+},\ q \leq 34$ ions colliding with argon has been discussed by Ali *et al.* [58]. Radiative stabilization was found to be of importance for the case of “asymmetric” doubly excited states, where the two excited electrons populate shells of different principal quantum number, $n << n'$. Hansen and collaborators [59] and Karim *et al.* [60] have recently calculated radiative and Auger decay rates for selected configurations of multiply excited ions. The *ab–initio* calculations of Vaeck and Hansen [59] predict that for increasing asymmetry of a doubly excited state, auto–ionization becomes less important and radiative transitions become possible in agreement with reference [58]. The close–coupling calculations of Chen and Lin [61] suggest a noticeable amount of radiative transitions (i.e. relatively large fluorescence yields) in certain quasi–symmetric configurations of high–lying, doubly excited Ar^{16+} states.

Very highly excited projectiles, such as generated in the case of incident Bi^{46+} ions (fig. 4.5b), offer a large number of auto–ionizing transitions between the many excited states of the hollow ion. These transitions can be combined to form an even larger number of possible relaxation cascades such that a rigorous theoretical treatment of the relaxation process is currently not possible. A simple relaxation scheme, based on intuition, basic features of emitted electron spectra, and wave function overlap arguments, has led to realistic final charge states of the relaxed projectile [14]. It consists of prioritizing possible relaxation steps and does not rely on detailed transition rates. For any configuration of the relaxing ion, the most likely next (Auger or radiative) transition is assumed to happen instantaneously and with unit probability.

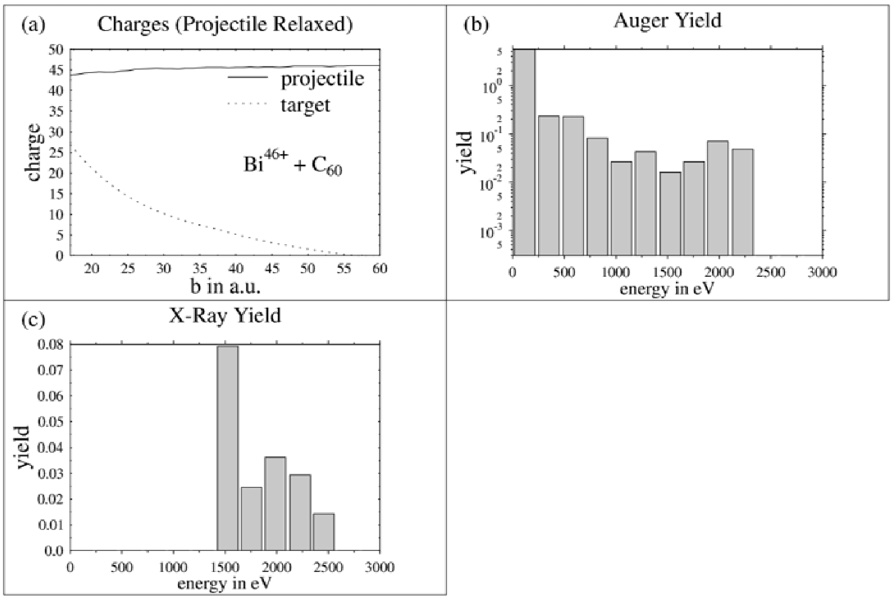

Figure 4.9. Results for 830 keV Bi^{46+} colliding with C_{60}, including downstream projectile relaxation. (a) Projectile and target charge states as a function of the impact parameter *b*. (b) Simulated Auger electron yield. (c) Simulated X-ray yield.

Results for incident 830 keV Bi^{46+} ions, including the downstream relaxation of the projectile are shown in fig. 4.9. As a consequence of the downstream relaxation process, most of the captured electrons get auto–ionized. This is easily seen by comparing the projectile charge states in fig. 4.9a with fig. 4.7b. The incident projectile charge effectively changes by no more than a few units. Auto–ionization is practically restricted to deexcitations that happen after the collision, as suggested earlier within a simple order–of–magnitude comparison of the collision time and typical Auger transition times (table 4.1). The simulated yields of emitted Auger electrons and X-rays in figs. 4.9b and 4.9c are accumulated over 234 eV–wide intervals of emitted electron and photon energies. These yields are normalized to the area perpendicular to the incident beam direction that the projectiles intersects with impact parameters between $b_{min} = 17$ and $R_1^* = 57.0$. For collisions in this impact parameter range, the total X-ray yield divided by total Auger yield amounts to 0.03.

2.7 Projectile kinetic energy gain

During a collision, a certain fraction of potential energy of the entire collision system may be transferred into kinetic energy of the projectile due to charge exchange processes. This energy can be calculated in two different ways. One possibility consists in integrating the net force between target and projectile along the trajectory. For the center–of–mass frame of reference, this amounts to integrating the force that governs the motion of the projectile of reduced mass along its trajectory. We define this systemic change in potential energy as *"nuclear" energy defect* Q_{nuc}, which is directly related to the motion of the reduced–mass projectile considered as an unstructured particle of variable charge. The net force is the sum of the direct Coulomb and image charge interactions between target and projectile and is provided as a function of time within the dynamical COM.

Obviously, due to energy conservation, Q_{nuc} is identical to the difference between the total electronic binding energy of the collision system before and after the collision. This *"electronic" energy defect* is denoted by Q_{el}. Since any COM–based simulation includes approximations of the complex dynamics of the multi–particle collision system that affect the coupling between nuclear and electronic degrees of freedom, the calculated values for Q_{el} and Q_{nuc} are expected to differ. The difference $|Q_{nuc} - Q_{el}|$ is indicative for the reliability of simulated translational kinetic energy gains. The electronic and nuclear energy defects for incident 46.2 keV Ar^{14+} ions are compared in reference [56].

In order to compare theory with measured projectile energy–gain spectra, the critical radii for the sequential capture of electrons may be related to energy defect values and to the number of electrons that are captured for a particular impact parameter. For impact parameters $b_i = R_{i+1}^*$, i electrons have been captured and the corresponding energy defects are $Q_{nuc}(b_i)$ and $Q_{el}(b_i)$. The simulated, discrete energy defects are folded with a Gaussian distribution G in order to correct for the finite experimental energy resolution. The full width at half maximum of G is adjusted to the resolution of the experiment. The simulated energy gain spectrum, differential in the projectile kinetic energy gain ΔE, is now given by the cross section

$$\frac{d\sigma}{d\Delta E} = \sum_i \sigma_i \, G(\Delta E - Q_i). \tag{4.6}$$

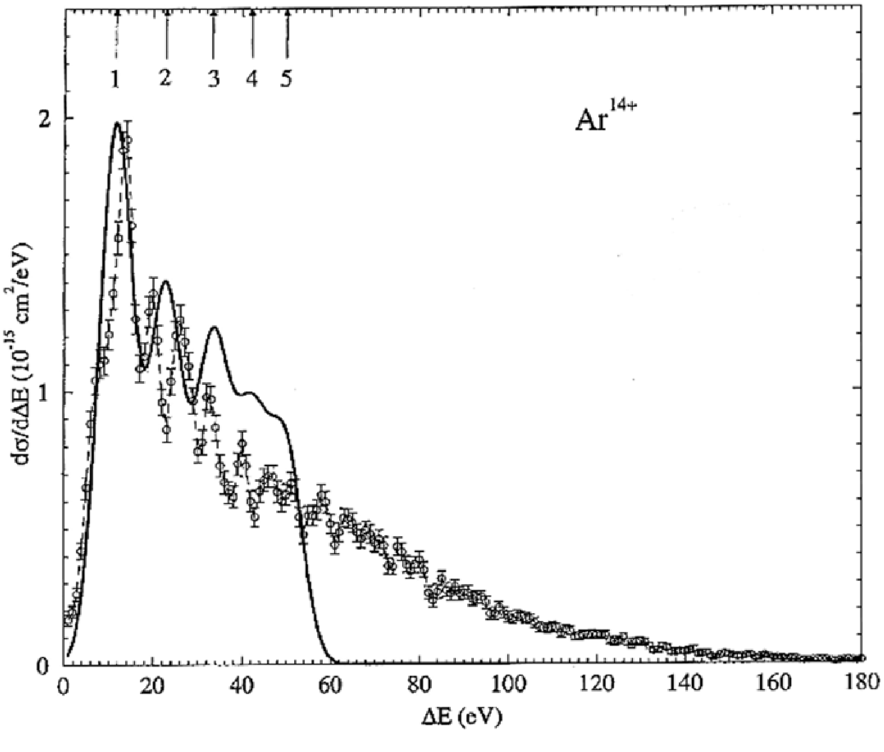

Figure 4.10. Simulated and measured projectile energy gain spectra for 46.2 keV Ar^{14+}–C_{60} collisions. The measured [55] and calculated [56] energy gain values and peak heights (cross sections) are absolute. The experimental errors in peak positions are typically ±0.5 eV. The arrows point to the calculated nuclear energy defects for the capture of 1, 2, 3, etc., electrons.

This method allows for the interpretation of peaks in measured spectra in terms of the corresponding number of captured electrons. In conjunction with the simulated projectile occupation changes, it also allows for the assignment of final projectile shells into which capture occurs at particular energy gains.

Fig. 4.10 contains an example for a measured differential energy gain spectrum from Selberg *et al.* [55] together with the simulated spectrum for the removal of a specific number of electrons from C_{60} [56]. Experimental and calculated spectra are absolute, both in intensity (peak heights) and energy gain. The calculated energy gains include the five lowest energy–gain peaks in fig. 4.10. In the overall trend, the lower part of the measured spectrum, which yields the dominant contribution to the total cross section, agrees well with the simulation. The calculated nuclear energy defects are indicated by numbered arrows and correspond to capture into specific projectile shells (1: capture into the $n = 12$ shell, 2: into $n = 11$, 3: into $n = 11$, 4: into $n = 10$, 5: into $n = 10$). The high energy gain region cannot be explained by the dynamical COM discussed in this chapter. Investigations are underway to understand this part of the kinetic energy gain spectra [62]. Similarly, even though reproducing the main features of the low–energy part of measured energy gain spectra on an absolute scale, the COM needs further refinement in order to more accurately agree with measured gains, e.g., for the capture of two electrons in fig. 4.10. A rewarding step in this direction could be the inclusion of projectile sub-shells nl, which are not resolved within the current version of the COM.

2.8 Projectile angular distributions

For slow highly charged ions colliding with C_{60}, simulations have predicted [45, 46] that the deflection function, i.e. the projectile scattering angle as a function of impact parameter, is characterized in its overall trend by two broad maxima that originate in the competition between attractive induced polarization and repulsive Coulomb interactions between the (charged) target and projectile. These maxima lead to strong measurable enhancements in the angle–differential scattering cross section that are usually referred to as 'Rainbow–Scattering'.

Walch *et al.* [12] have measured the angular distributions of 2.5 keV Ar^{8+} projectiles following the capture of 1 to 5 electrons from C_{60}. They determined the number of captured electrons by measuring simultaneously the scattered projectile and a charge-state-analyzed intact C_{60}^{i+} recoil ion. An experimental angle resolution of ≈ 0.01 degrees pointed to a potentially measurable prominent structure in the angle–differential cross section. The observed angular distributions in fig. 4.11 show a strong increase of the deflection angle with the number of electrons removed from C_{60}, due to the increasing Coulomb repulsion between positively charged collision partners.

A comparison with calculations based on the dynamical COM [12] shows good agreement only if the influence on the projectile trajectory by the large polarizibility of the C_{60} target is taken into account. This means that, due to the large polarizability of C_{60}, the trajectory of a highly charged ion captur-

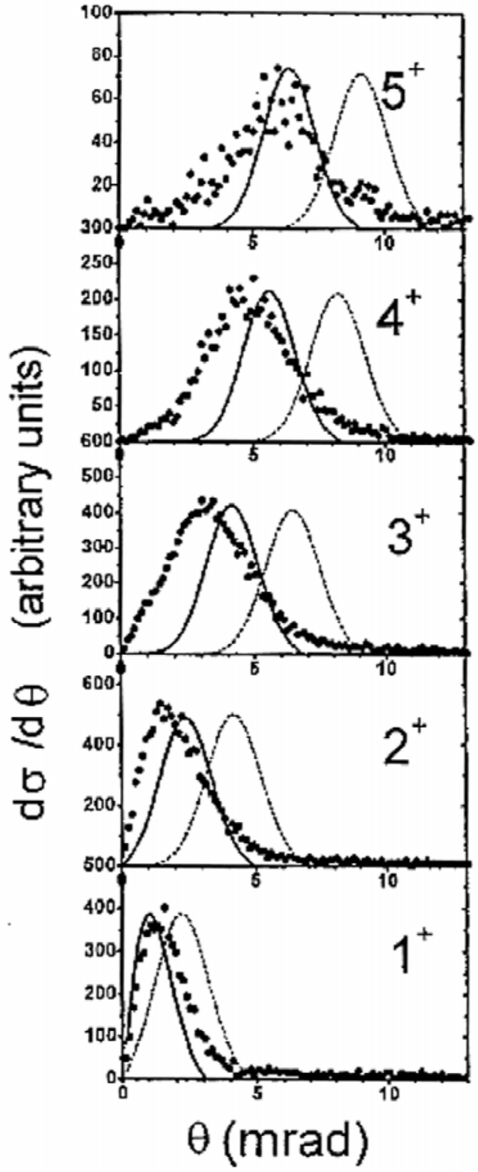

Figure 4.11. Angular distributions for the capture of i=1...5 electrons from C_{60} by 2.5 keV Ar^{8+} ions [12]. Each figure is labeled by $i+$. Θ is the deflection angle. The solid curves are dynamical COM calculations including target polarization. The dotted curves are calculated without this polarization.

ing electrons in the "soft" over-barrier region of impact parameters is affected measurably by the induced target polarization. This effect is a truncated analog of the image charge acceleration of highly charged ions incident on solid surfaces [39].

Calculated angular distributions, including the attractive self–image interaction of the projectile with the dipole it induces in the target, are shown in fig. 4.11 as solid lines. The same simulations without the induced polarization effects are shown as dotted lines. The agreement between the COM simulation and experiment in the location of the maxima is remarkable, showing that the model describes the basic interaction very well. The effect of the induced target polarization on the deflection of the projectile is clearly observed in all cases shown. It offers the interesting prospect of making the collective dielectric response of the cluster target observable in scattering experiments.

Since, classically speaking, the scattering angle is a function of the impact parameter, it also allows us to investigate how closely the projectile can pass by the target without disintegrating the C_{60} cage. This investigation is similar to the question of how much total energy is transferred to the C_{60} internal degrees of freedom as a function of impact parameter.

An alternative, interesting effort to calculate angle–differential scattering cross sections in HCI–C_{60} collisions has been made by Sakurai and Bárány [63]. This approach uses approximated Landau–Zener transition rates and classical potential scattering theory.

3. Collisions of Highly Charged Ions with Surfaces

The ideas of the previous section on multiple electron capture in soft collisions with C_{60} apply equally well to the formation of multiply excited projectile ions in surface collisions with incident HCIs of a sufficiently small component of the asymptotic incident velocity $|v_{\perp}^{0}|$ along the surface normal $\hat{e}_z$. As for collisions with fullerenes, at distances of typically 20 to 50 atomic units from the target surface, the potential barrier between the HCI and the target drops below the target Fermi level and initiates the efficient capture of target electrons, resulting in the formation of a hollow projectile ion.

However, due to the interaction between the positively charged HCI and the negative image charge it induces in the surface, the ion is accelerated towards the surface and hits the surface at a speed in excess of $|v_{\perp}^{0}|$. Even for the idealized case $v_{\perp}^{0} \rightarrow 0$, that is for a projectile that starts out with no perpendicular velocity component at a very large distance from the surface, the image charge acceleration brings the projectile ion in very close contact with the surface and results in the "destruction" of the HCI. Thus, in contrast to large–impact parameter collisions with gaseous targets, for collisions with surfaces the COM needs to be extended in order to include those interaction mechanisms that dominate close to the surface. In this context, "close" can be specified by ion–surface distances at which the hollow ion starts getting destroyed due to significant overlap of the outermost populated states of the multiply excited ion and the electronic charge density of the surface.

3.1 Projectile motion and electron transfer at large distances from the surface

3.1.1 Projectile motion. The motion of the scattered projectile can be described by solving Newton's equation,

$$\Delta\vec{v} = \frac{\vec{F}(q_p, \vec{R})}{m_{\text{nuc}}}\Delta t\,, \tag{4.7}$$

where $\vec{R}$ denotes the position of the projectile nucleus with respect to a fixed point in the top–most lattice plane of the target. The force acting on the projectile,

$$\vec{F}(q_p, \vec{R}) = -\left(\frac{q_p(R)}{2(R - z_{\text{im}})}\right)^2 \hat{e}_z + \vec{F}_{TFM}(\vec{R}), \tag{4.8}$$

consists of two terms, the long–range interaction of the charged projectile with the image charge it induces in the surface and a short–range force $\vec{F}_{TFM}$ that represents all interactions of the projectile with individual target atoms in terms of a sum over binary forces between the projectile and target atoms localized at the target lattice points. The binary interactions are modeled as atomic Thomas-Fermi-Molière (TFM) potentials [64] and do not depend on the net projectile charge state $q_p = q_{nuc} - \sum_n a_n$. The unit vector $\hat{e}_z$ points along the surface normal, which is parallel to the z axis. The electronic coordinate $z = 0$ coincides with the top–most lattice plane. $z = z_{im}$ denotes the position of the image plane. Due to its dependence on $q_p(\vec{R})$, the projectile motion is coupled to its occupation evolution $\{a_n(t)\}$. Mass and charge of the projectile nucleus are designated as m_{nuc} and q_{nuc}. Recoil effects in close encounters with individual target atoms can be included by switching to a binary collision mode at distances below one–half of a lattice constant [17]. The inclusion of target recoil leads to a closer approach of the projectiles to the first bulk layer of the target as compared to a rigid crystal.

3.1.2 Kinetic energy gain. As discussed earlier for the case of HCI - C_{60} collisions, the self image interaction accelerates the projectile on the incident trajectory and thus increases its kinetic energy. Simulations as well as recent experiments [19] show that the neutralization of the HCI is completed prior to its reflection for a wide range of initial projectile charge states, leading to primarily neutral projectiles. Under the assumption that all reflected projectiles are neutral, and therefore do not experience any further image charge interactions that could change their kinetic energy close to the surface, the kinetic energy increase of the projectile ion is determined by the neutralization steps on the incident trajectory. This means that measurements of the kinetic energy gain are primarily sensitive to the distant interactions with the surface. In fact, an incident ion has accumulated over 70 % of its net kinetic energy gain by the time it reaches the critical distance R_1^* for over–the–barrier capture of the first target electron. Knowing that the complicated interaction dynamics at close distances to the surface is of little influence on the projectile kinetic energy gain, it is reasonable to first compare any model for HCI - surface interactions with measured kinetic energy gains, before proceeding to observables that are determined by the more intricate interaction dynamics at close distances.

Image energy gains of an HCI impinging on metal surfaces are characterized by an approximate $q^{3/2}$–increase with the initial projectile charge state q [65–67]. Within the COM, a lower limit for the kinetic energy gain can be deduced by assuming that the projectile is instantaneously and completely neutralized at the first critical distance $R_1^* \simeq \sqrt{8q+2}/(2W)$ [68], where W is the target work function. The energy gain for large q is then given by the expression

$$\Delta E = \frac{q^2}{4R_c} = \frac{Wq^{3/2}}{4\sqrt{2}}. \tag{4.9}$$

We refer to this estimate as *"simple COM"*. According to this result, the ratio $\Delta E/W$ does not depend on the target material.

The simple COM can be improved by letting one electron transfer to the HCI each time the over–barrier condition is fulfilled at consecutive critical radii, R_i^*, for the first, second, etc. capture. This version of the COM is called the *"staircase model"* [65]. In contrast to the dynamical COM (cf. section 4.2.1), in the simple and staircase model the charge transfer current is quantized. For energy gains of Xe^{q+} projectiles on an Al surface, the staircase model almost coincides with the dynamical COM for all initial charges q, and the simple model predicts, as expected, lower energy gains for all q (fig. 4.12). Except for the highest charge states, where the measured kinetic energy gains merge into a "plateau", both, the staircase and dynamical COMs agree with the experimental kinetic energy gains of Winter *et al.* [69], even though the more elaborate dynamical COM employs transition rates that depend on the width and depth of the potential saddle. Winter *et al.* deduced the energy gains from the difference of the measured asymptotic angles of incidence and reflection of the ion beam [67]. The simple model underestimates the measured energy gain, except for the highest charge states, where agreement with the experiment is fortuitous. As far as we know, the initial charge state q at which the experimentally observed plateau appears has not yet been reliably calculated. Fig. 4.12 also shows that the staircase COM calculation of Lemell *et al.* [65] agrees with our dynamical COM results [38].

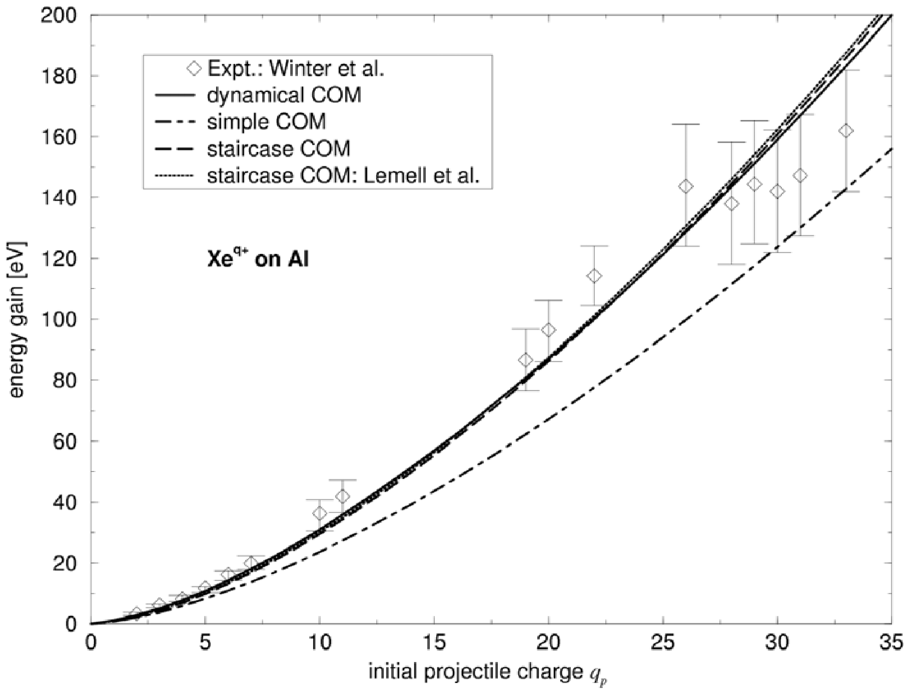

Figure 4.12. Experimental [69], simulated staircase COM results [65], and simulated energy gains from the dynamical COM [38] for Xe^{q+} (3.7 q keV, $1.5°$) on an Al surface. The simple model assumes instantaneous complete neutralization at the first critical distance R_1^* and sets a lower boundary for projectile energy gains. The staircase COM instantaneously transfers one charge unit each time the over–barrier condition is fulfilled. In the dynamical COM continuous charge currents flow between projectile and surface.

Kurz *et al.* [26] have analyzed total electron yields for very high charge states as a function of the inverse projectile velocity. The data of Kurz *et al.* for Xe$^{q+}, q = 34 \ldots 50$ and Th$^{q+}, q = 61 \ldots 79$ on gold surfaces under perpendicular incidence provide, if at all, weak evidence for a deviation of the energy gain from the $q^{3/2}$–proportionality (fig. 4.13).

3.2 Electron transfer and emission at smaller distances from the surface

As the HCI moves closer to the topmost surface layer, electrons that were previously captured into highly excited states get increasingly disturbed and eventually lost. Lacking a detailed *ab-initio* description, models have been developed in order to identify and represent the most prominent features of the interaction scenario at small distances. Fig. 4.14 illustrates the various interaction

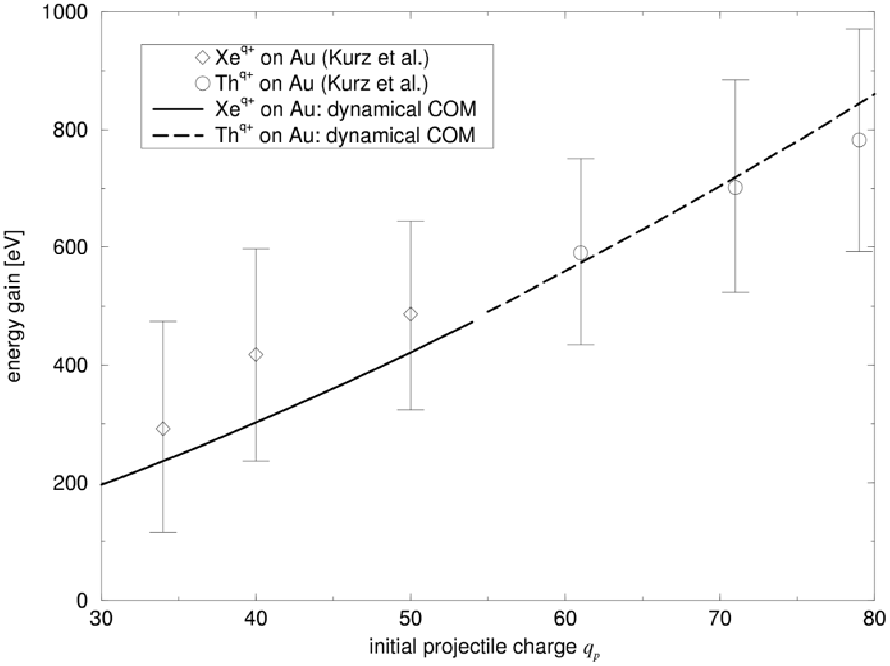

Figure 4.13. Experimental [26] and simulated dynamical COM data [38] for very high charge state ions impinging on polycrystalline gold.

stages during the ion's approach to the surface. Interactions in the near-surface zone are strongly influenced by target conduction band electrons that pour into the Coulomb well around the projectile core. The most prominent near–surface interaction mechanism is the direct transfer of electrons from target states into inner shells of the HCI (often referred to as "side feeding (SF)" [22, 70–72]) and the loss of loosely bound projectile electrons due to additional screening enforced by the tightly packed induced charge cloud (so called "peeling off" (PO)) [20, 73]. Simple illustrations of these basic interactions mechanism are shown in fig. 4.15. We emphasize that the separate investigation of largely simplified interaction rates for intuitive interaction modes, such as SF, PO, RC, and RL is justified only by the complexity of the many–electron dynamics involved. Since all of these mechanisms share a common cause, namely the strong perturbation of target (projectile) electrons by the projectile (target), modeling the intuitive mechanisms separately bears the risk of over-counting. The quality of these models therefore can be assessed only in comparison with experimental data.

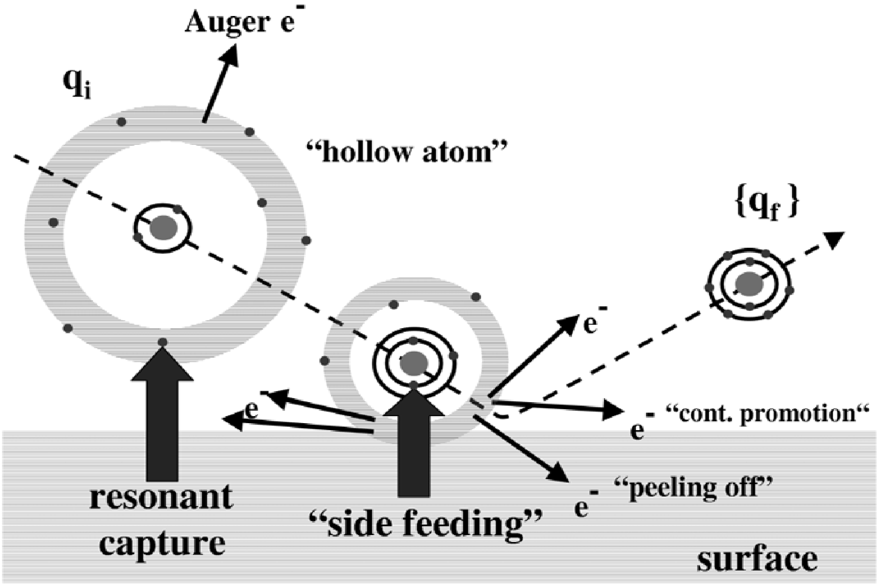

Figure 4.14. Sketch of the interaction scenario for the neutralization and reflection of an incident highly charged ion near a metal surface (see text).

3.2.1 Side feeding.

For incident ion energies of up to several 100 keV and for a wide range of initial ion charge states and target materials, experiments on the final charge distribution of reflected projectiles have shown that the vast majority of the projectiles emerges in a neutral charge state [74–76]. Furthermore, it has been well known for more than a decade that the above-surface auto–ionization cascade does not allow for the full relaxation of the projectile on the incoming part of its trajectory. Simple estimates for Auger transition rates have suggested that this "bottle neck" originates in individual Auger relaxation steps of the hollow projectile that are slow compared with the time available between the second electron capture by the projectile and its close contact with the surface. This has led to the suggestion that tightly bound projectile levels are predominantly and very rapidly filled with target electrons in a region of strong overlap with the target electron distribution [17, 19, 22, 71, 77, 78]. This fast electron transfer mechanism was termed "SF", and was vaguely associated with the resonant transfer of localized, tightly bound target electrons.

Soon afterwards, it also became clear, that the SF mechanism leads to complete neutralization even in cases where the energies of projectile and target inner shells do not match and where, in consequence, an interpretation in terms of the resonant electron transfer fails. This stimulated the investigation of rapid

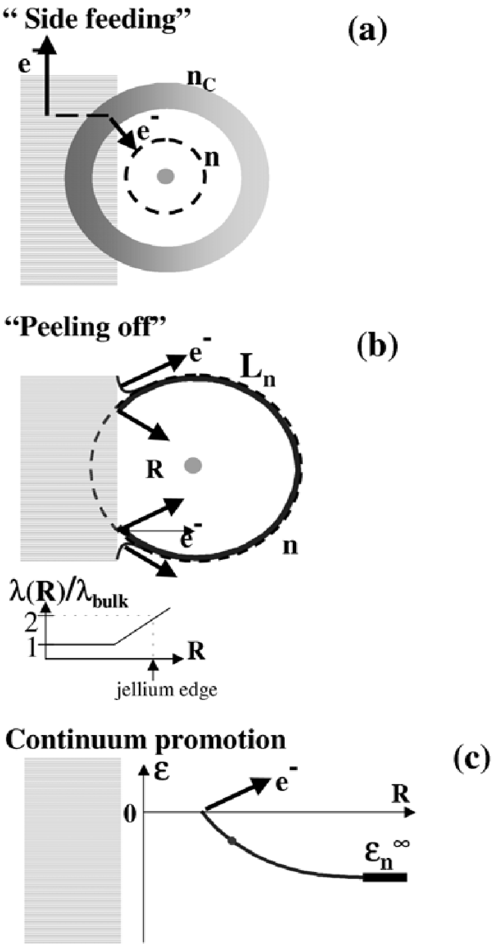

Figure 4.15. Illustrations of the near–surface electronic interaction mechanisms side feeding (a), peel–off (b), and continuum promotion (c). (b) also shows the assumed variation of the screening length λ as a function of the ion–surface distance R with respect to the bulk screening length λ_{bulk}.

inner shell transfer mechanisms that involve more than one active electron. In such a transfer, non-resonant projectile states become accessible into which an active electron can be captured. The active electron can restore the overall energy balance by transferring energy to a second electron (or an ensemble of other electrons, so-called “plasmons”). During this process, the second electron is excited or emitted. We introduced such an inner-shell population mechanism as an *XCC*-like process [48]. As a matter of convenience, we refer to it as SF. X designates an inner shell of the projectile $(K, L, M, \ldots)$. This two-electron process is similar to regular Auger processes. However, the participating two electrons initially belong to the induced valence–band charge cloud (C) surrounding the projectile ionic core near and below the surface. LCC rates Γ_L^{SF} have been approximated by LCV processes [70] where a charge cloud electron (C) fills the L-vacancy while exciting a plasmon or an electron-hole pair in the valence band (V). Since C electrons remain localized about the ionic core, approximated *XCC* rates Γ_n^{SF} can be calculated in analogy to ordinary intra-atomic Auger rates [79]. In our dynamic simulation, we found that the LCV rates specified in reference [70] for N embedded into Al are too slow to explain measured final charge state distributions of reflected projectiles.

Ion-surface interaction models that include SF and other interactions close to the surface (in addition to the basic assumptions of the dynamical COM for distant interactions) include a variety of assumptions and adjustable parameters. In order to enable a meaningful comparison with experimental results, model calculations need to be performed with a fixed set of adjusted parameters for a variety of measured observables and of as many collision systems as possible. For this reason, model *XCC* SF rates were constructed in an attempt to include as much plausible physics as possible in their analytic form. These rates may then be fine–tuned by fitting experimental results [17, 48]. For all collision systems and all localized atomic levels $1 \leq n \leq n_{loc}$, we assume a single base rate $\Gamma_0^{SF} = 0.01 \approx 4 \cdot 10^{14}\, 1/s$. For each shell n, Γ_0^{SF} is multiplied by the number of n-shell vacancies N_n^{vac} and a factor that models the spatial variation of Γ_n^{SF},

$$N_n^{ol}(R) = \begin{cases} \frac{V_n^{\mathrm{ol}}(R)}{V_n} & \text{if } R > z_j - \langle r \rangle_n \\ 1 & \text{otherwise} \end{cases} . \tag{4.10}$$

We account for the strong $(1/\Delta n)^{3.46}$-scaling of Auger rates $\Gamma_{n',n}^{AI}$ with the difference Δn between participating levels [20] (eq. (4.4)) and arrive at the LCV rate

$$\Gamma_n^{SF}(R) = \Gamma_0^{SF} q_c\, N_n^{vac} N_n^{ol}(R) \left(\frac{n_{\mathrm{loc}} + 1 - n_L}{n_{\mathrm{loc}} + 1 - n} \right)^{3.46} \tag{4.11}$$

for side feeding into projectile shell n. V_n^{ol} is the part of the orbital volume of level n, $V_n = 4\pi/3\ \langle r \rangle_n^3$, that overlaps with the metal electron distribution. q_c denotes the charge of the ionic core. For calculating this overlap, the metal electron distribution is supposed to extend to the (assumed planar) jellium edge located a distance z_j in front of the topmost layer of lattice points. At the jellium edge, the density of conduction electrons is $1/2$ of the bulk electron density. According to this model $N_n^{ol}(R)$ vanishes for distances $R > \langle r \rangle_n + z_j$. If the projectile has penetrated the jellium edge by more than the orbital radius $\langle r \rangle_n$, we assume $N_n^{ol}(R)$ to remain constant at the value 1.

3.2.2 Peeling off.

Outer orbitals that were resonantly populated at large ion–surface distances with typical orbital radii $\langle r \rangle_n \simeq R_{crit}$ are increasingly disturbed as the HCI approaches the bulk. By modeling PO as the instantaneous loss of an electron as soon as a certain fraction of the HCI orbital volume overlaps with the surface electron distribution, our simulation results for the final charge-state distributions of the projectile disagreed with experiment [74, 75, 80], since peeled off electrons are immediately replenished by RC. In contrast to previously implemented *instantaneous* PO mechanisms which become effective at the moment the HCI enters the bulk region [73, 81], we examined the influence of a *dynamic* PO on the speed of the electron transport from outer projectile levels into inner levels during the entire projectile–surface interaction [48].

We modeled PO by interpolating smoothly between the (remote) vacuum region and the bulk limit. We assumed that near the surface, for $R < \langle r \rangle_n + z_j - \lambda_{scr}$, when the electron has "lost touch" with the ionic core due to screening, the outermost orbital is likely to move to the valence band continuum if its radius $\langle r \rangle_n$ exceeds the screening length

$$\lambda_{scr}(R) = \lambda_{scr}^0 \left(\frac{\max(R, 0)}{z_j} + 1 \right). \tag{4.12}$$

The screening length is assumed to reach its bulk value λ_{scr}^0 at $R = 0$. Above the first bulk layer, $\lambda_{scr}(R)$ increases linearly in R and equals $2\lambda_{scr}^0$ at the jellium edge $R = z_j$. Due to the nonlinear response of the surface electron distribution to the nearby HCI, the linear scaling in R, the neglect of a variation with the incident projectile charge q, and the particular choice of the slope, Eq. (4.12) can represent only a crude estimate for the dependence of λ_{scr} on q, n, and R.

Our model PO rate,

$$\Gamma_n^{PO}(R) = a_n \frac{N_n^{ol}(R)}{T_n} \frac{2\pi \langle r \rangle_n}{L_n(R)} \Theta(\langle r \rangle_n - \lambda_{scr}(R)), \tag{4.13}$$

is composed of several parts. Similar to the derivation of the RL rate in [20], our base rate is given by the inverse orbiting time T_n of an electron in an unperturbed orbital. As in eq. (4.11), we reduce T_n by a volume factor $N_n^{ol}(R)$. The term $L_n(R)/(2\pi \langle r \rangle_n)$ corrects T_n to yield the "reaction time" for an atomic electron. We assumed that an electron which is captured at $R - z_j = \langle r \rangle_n$ and enters an atomic orbital does not get perturbed by the target electron gas until it has covered the distance $L_n(R)$. This period decreases with the ratio of the vacuum section $L_n(R)$ of the classical orbital above z_j and its circumference $2\pi \langle r \rangle_n$.

The unit step function Θ in eq. (4.13) disables PO for levels with shell radii $\langle r \rangle_n$ smaller than the screening length $\lambda_{scr}(R)$.

In the present simulation, PO rates were introduced to replace RL rates if $\langle r \rangle_n < \lambda_{scr}(R)$. Both, PO and RL, represent resonant electron flow into empty band states and could not be distinguished in a precise theory.

3.2.3 Continuum promotion (CP). As the HCI approaches the surface, due to the action of the repulsive projectile image potential $V_{im,p}$ and the mutual screening of projectile electrons, atomic levels are shifted upwards with respect to their asymptotic values ε_n^∞. As the orbital energies $\varepsilon_n = \varepsilon_n^\infty + V_{im,p}$ reach the ionization threshold, electrons in shell n are detached from the projectile, i.e., have effectively been promoted (and lost) to the continuum. We assume immediate electron loss due to CP as soon as $\varepsilon_n > 0$.

The energies $\{\varepsilon_n^\infty\}$ for a given instantaneous occupation $\{a_n(\vec{R})\}$ of projectile shells can be evaluated by using a standard atomic structure program [47].

3.3 Evolution of projectile level populations

3.3.1 Rate equations for the projectile population. During the HCI – metal surface interaction the populations a_n of projectile shells with principal quantum number n vary as a function of time. They are given as solutions of a system of rate equations of the form [48]

$$\begin{aligned}
\frac{da_n}{dt} &= \theta(A_n - a_n)\Gamma_n^{RC} - a_n\Gamma_n^{RL} \\
&+ \sum_{n'>n} \Gamma_{n',n}^{AI} - 2\sum_{n'<n} \Gamma_{n,n'}^{AI} \\
&+ \theta(A_n - a_n)\Gamma_n^{SF} - a_n\Gamma_n^{PO} + \Gamma_n^{CP} \\
&- \delta_{n,M}\Gamma^{CK} - \delta_{n,L}\Gamma^{sCK} \\
&+ (\delta_{n,K} - \delta_{n,L} - \delta_{n,M})\, a_L a_M \Gamma^{KLM} \, . \qquad (4.14)
\end{aligned}$$

We have encountered the processes in the two first lines of eq. (4.13) before (cf. section 4.2.1). For ion–surface interactions, these two lines describe the interaction scenario at intermediate and large distances R. They correspond to the "traditional" COM [20] and include the rates for resonant capture, Γ_n^{RC}, resonant loss, Γ_n^{RL}, and Auger transition rates $\Gamma_{n',n}^{AI}$. As in section 4.2.1, $\Gamma_{n',n}^{AI}$ describes only fast Auger relaxation steps that require at least two equivalent active electrons in an outer shell. Slow Auger processes do not contribute to the relaxation of the excited projectile prior to its impact on the surface. The Auger rates in eq. (4.13) include statistical weights in order to take the variable number of electrons in the initial and final active shells, n and n', into account [48]. θ is the unit step function and $\delta_{n,n'}$ the Kronecker symbol.

For the simulations discussed below, we have added the terms in the third, fourth and fifth line, including the rates for SF, PO, and CP, Γ_n^{SF}, Γ_n^{PO}, and Γ_n^{CP}. In general, we do not resolve the populations in particular projectile subshells. For the L-shell and the applications to very slow collisions discussed below, however, we calculate the $2s$ and $2p$ binding energies and keep track of the respective subshell populations. We assume that the $2p$ level is preferentially populated via Auger ionization (AI) and side–feeding processes, as suggested by its higher degeneracy and its lower binding energy. With increasing occupation, L-shell relaxation via LLM Coster–Kronig (CK) and LLL super CK (sCK) transitions becomes energetically possible and proceeds by one and two orders of magnitude faster, respectively, than other Auger processes [82]. The rates for CK, sCK, and KLM Auger transitions are included in the last line of eq. (4.13).

3.3.2 Monte-Carlo Sampling.

The time integration of eqs. (4.7) and (4.13) for the level occupations $\{a_n(t)\}$ and the projectile trajectory $\vec{R}(t)$ is performed by Monte-Carlo sampling over a large number (of the order of 5000) incident projectiles. Starting at a random position just above the ($R = R_{crit}$)-plane, the HCI moves along its trajectory from a position $\vec{R}(t_i)$ to $\vec{R}(t_{i+1})$ within a short time interval Δt_i. At each time t_i, separate values Δt_i for each transition type $X \in \{$AI,RC,RL,SF,PO$\}$ are drawn from an exponential random number distribution

$$\Xi(\Delta t) = [\int_0^\infty \exp(-\Gamma^X \tau) d\tau]^{-1} \exp(-\Gamma^X \Delta t). \tag{4.15}$$

The physical process X supplying the smallest Δt_i is chosen to take place, and all variables, such as configuration energies and occupations, are updated according to the change in $\{a_n(t)\}$ during Δt_i. The projectile, in an electronic configuration given by eq. (4.13), is then moved from $\vec{R}(t_i)$ to $\vec{R}(t_{i+1})$ by the force given in eq. (4.8). Next, the same procedure starts over again leading to time step t_{i+2}, etc. Should the smallest drawn Δt_i be large (we assumed larger than one), the projectile is moved from $\vec{R}(t_i)$ to $\vec{R}(t_{i+1})$ without any electronic transition taking place.

3.4 Comparison with Measurements

Having outlined the basic model assumptions in the extended dynamical COM, we proceed by comparing our simulated results with various experiments. We have already confirmed in section 4.3.1.2 that our model reproduces measured projectile energy gains over a large range of charge states of the incident ion and for different projectile and target species. However, we have only included distant ion–surface interactions (corresponding to the two first lines in eq. (4.13)) and simply assumed complete neutralization of the projectile at the surface. With respect to the significant modifications given by the third and fourth lines in eq. (4.13), this agreement cannot necessarily be expected for simulations of projectile kinetic energy gains that include the *entire* trajectory of the reflected projectile [38, 48].

The comparison with experiments in section 4.3.1.2 was facilitated by the fact that the kinetic energy gain is mainly accumulated at large ion-surface separations. The present calculation of energy gains within the extended COM includes the entire trajectory of the reflected projectile and, in particular, describes the rapid neutralization of the projectile near the surface. Changes in the SF or PO rate were found to sensitively affect the dominant charge state of the reflected ion and, therefore, the net kinetic energy gain of the projectile that accumulates along its reflected trajectory. The results discussed below were obtained with model transition rates and adjustable parameters that also reproduce the measured kinetic energy gains.

3.4.1 Final charge state distributions. After the reflection of highly charged ion beams on surfaces, high fractions of completely neutralized projectiles, typically well above 90%, have been observed, even on insulating targets [74–76]. The remaining charged fraction of the measured final projectile charge-state distributions $\{q_{final}\}$ overwhelmingly consists of singly charged positive and negative ions. The traditional COM [20], does not allow for the efficient neutralization of the incident HCI, due to the "bottle–neck" problem mentioned above. Burgdörfer *et al.* [22] have included a resonant L-shell filling mechanism to comply with measured final charge states. The extended COM discussed in this chapter reproduces the strong trend towards neutrality in the q_{final}-distribution while, in addition, keeping agreement with other observables.

Fig. 4.16 shows the simulated charge fractions $q_{final} = 0, 1$, and 2 of the final charge–state distributions for ground state (gs) H-like ions and metastable (mt) He-like ions C^{q+}, N^{q+}, and O^{q+} in $(1s, 2s)$ configurations, impinging with $E_{kin} = 13q$ eV and a grazing angle of $\Theta = 5°$ on Al(111). The simulated fractions are recorded for reflected projectiles which have passed the first capture distance R_1^*. After this point, less than 0.1% of the beam still exhibits the original K-shell vacancy which eventually causes re-ionization. Also shown are measurements by Folkerts *et al.* [75] for O^{q+} ($3 \leq q \leq 8$) at $E_{kin} =$ 3.75 keV/amu on Au(110) under surface channeling conditions. Note that the simulations were applied to different projectile types containing a single K-shell hole while the experiment was performed only for O^{q+}-projectiles with K-shell vacancies for $q \geq 7$. Simulations for incident projectile ions with a filled K-shell leads to slightly higher degrees of neutralization.

Neglecting the influence of the projectile kinetic energy, the measured charge-state distributions in fig. 4.16 agree well with our simulation results. Shifting the final charge state fractions of the metastables by $\Delta q = +1$ towards the

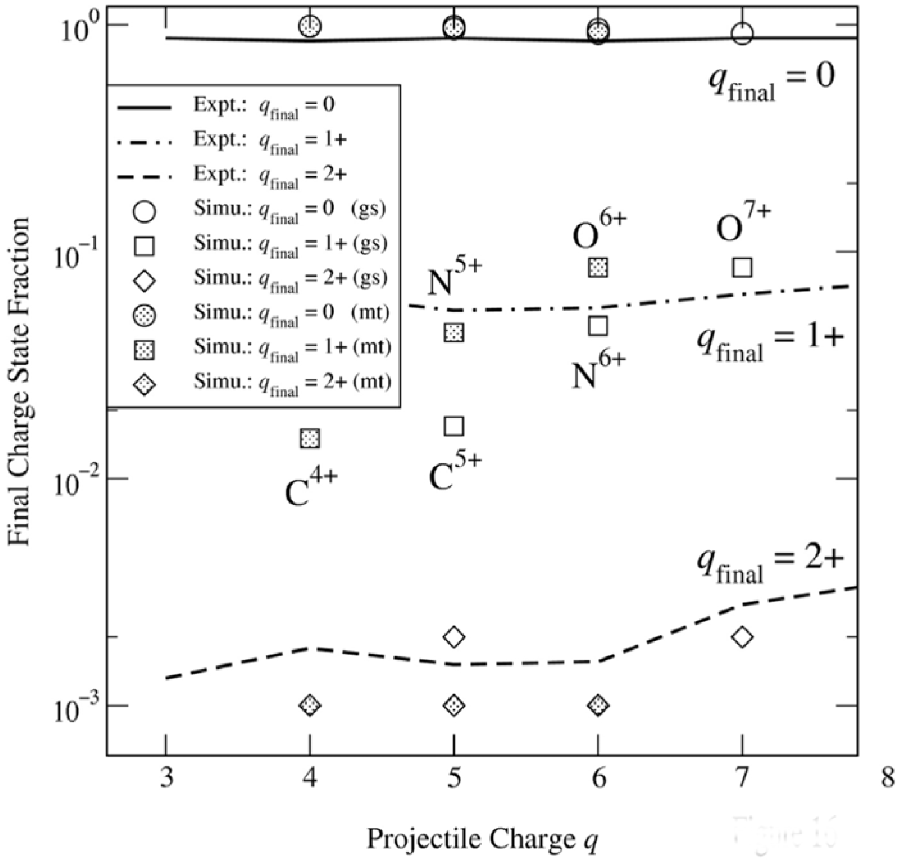

Figure 4.16. Final charge state fractions. The lines represent experimental data by Folkerts *et al.* [75] for O^{q+} impinging at $E_{kin} = 3.75$ keV/amu on Au(110) under surface channeling conditions. The simulation results [48] are given for H-like (gs) and He-like ($1s2s$) metastable (mt) C^{q+}, N^{q+}, and O^{q+} ions scattering with $E_{kin} = 13q$ eV and $\Theta = 5°$ off an Al(111) surface.

right, the data points for the H-like and He-like counterparts almost coincide for $q_{final} \leq 1$. This means that the distribution of q_{final} depends strongly on the nuclear charge and is rather insensitive to the initial L-electron.

3.4.2 Low-energy electron emission. Electron emission originates from various processes. Apart from auto–ionization, SF and CP may contribute to the emitted electron yield. In fig. 4.17a we show experimental and simulated electron emission spectra for N^{6+} interacting with an Al(111) surface, incident under $\Theta = 45°$ with kinetic energies E_{kin} of either 80 eV or 10 eV. For

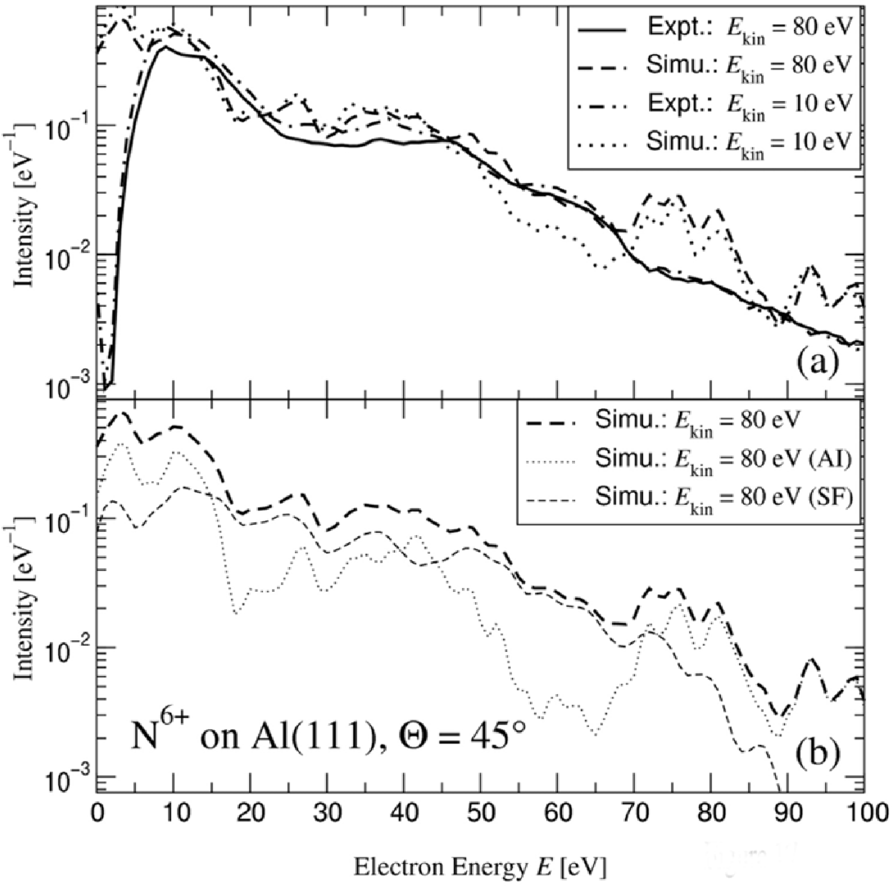

Figure 4.17. Low-energy electron spectra of N^{6+} incident under $\Theta = 45^\circ$ on an Al(111) surface. Experimental and simulated spectra for incident energies $E_{kin} = 80$ eV and 10 eV (a). (b) SF and AI contributions to the $E_{kin} = 80$ eV spectrum.

these low incident kinetic energies, the simulated image energy gains amount to $E_{gain} = 17.1$ eV and 16.3 eV, respectively. The simulated data have been convoluted with the spectrometer resolution of 0.7% [48].

Vanishing spectrometer transmission and stray magnetic fields aggravate the detection of electrons at the lowest displayed energies, and only the experimental results for emitted electron energies above $E > 20$ eV are reliable. The spectra in fig. 4.17 and all the following plots are normalized to the integral K-Auger intensity. At electron energies $E > 10$ eV, the simulated spectra exhibit reasonable agreement with the experiment for both energies of the incident projectile. Additional structures in the simulated spectra are reminiscent

Table 4.2. Number of electrons emitted per projectile, γ, for N^{6+} ions, incident with kinetic energy E_{kin} on Al and Au surfaces.

system	E_{kin}/eV	γ		
N^{6+} + Al	10	4.9	experiment	[48]
	10	5.7	simulation	[48]
	80	4.3	experiment	[48]
	80	5.8	simulation	[48]
N^{6+} + Au	90	8.6 $\pm$3.4	experiment	[81]
	90	9.8	experiment	[85]
	90	15.4 (AI:7.6, SF:6.6, CP:1.2)	simulation	[48]

of our simplified evaluation of transition energies which considers only ground state configurations for shells $n > 2$, neglects angular momentum coupling, and the perturbation and hybridization of ionic levels near the surface [83, 84]. Fig. 4.17b displays the contributions of AI and SF to the simulated spectrum for 80 eV incident ions. While the SF mechanism produces a comparatively smooth spectrum in the region $E < 90$ eV, AI transitions generate structures below 20 eV, which we associate with the early stage of projectile relaxation above the surface, where small Δn steps between Rydberg states prevail. In the same interaction phase, highly-excited configurations may also emit L-Auger electrons, which enhance the emission of more energetic electrons. CP does not contribute noticeably to the electron yield in fig. 4.17a.

The estimated total number γ of electrons emitted per incident ion is obtained by integration over all emitted electron energies. Integrating the spectral yields in fig. 4.17a above 20 eV leads to yields of $\gamma = 5.7$ and 5.8 emitted electrons per incident ion for the simulated spectra and to $\gamma = 4.9$ and 4.3 for the experiments with $E_{kin} = 10$ eV and 80 eV, respectively (table 4.2).

Low-energy Auger spectra for N^{6+} colliding with an Au surface at perpendicular incidence with E_{kin} ranging from 90 eV to 60 keV recently have been published by Niemann *et al.* [81]. Their total emission yield for $E_{kin} = 90$ eV, $\gamma = 8.6 \pm 3.4$, agrees well with their simulated yield of $\gamma_{AI} = 9.8$ for mere auto–ionization. With a different technique, Eder *et al.* [85] measured a yield of $\gamma = 9.8$ under similar scattering conditions. For the same collision system, the extended COM simulation including dynamic PO, CP, and SF mechanisms provides electron yields $\gamma_{AI} = 7.6$ for Auger emission, $\Gamma_{SF} = 6.6$ due to SF, and $\Gamma_{CP} = 1.2$ due to CP [48]. These values add up to a total yield, $\gamma = 15.4$, including contributions from $E < 20$ eV (table 4.2). The discrepancy with Eder *et al.* and Niemann *et al.* might be rooted in the experimental difficulty to measure low-energy electrons ($E < 20$ eV), which produce the greatest contribution to γ, as well as in the necessary simplifications embedded in the simulation.

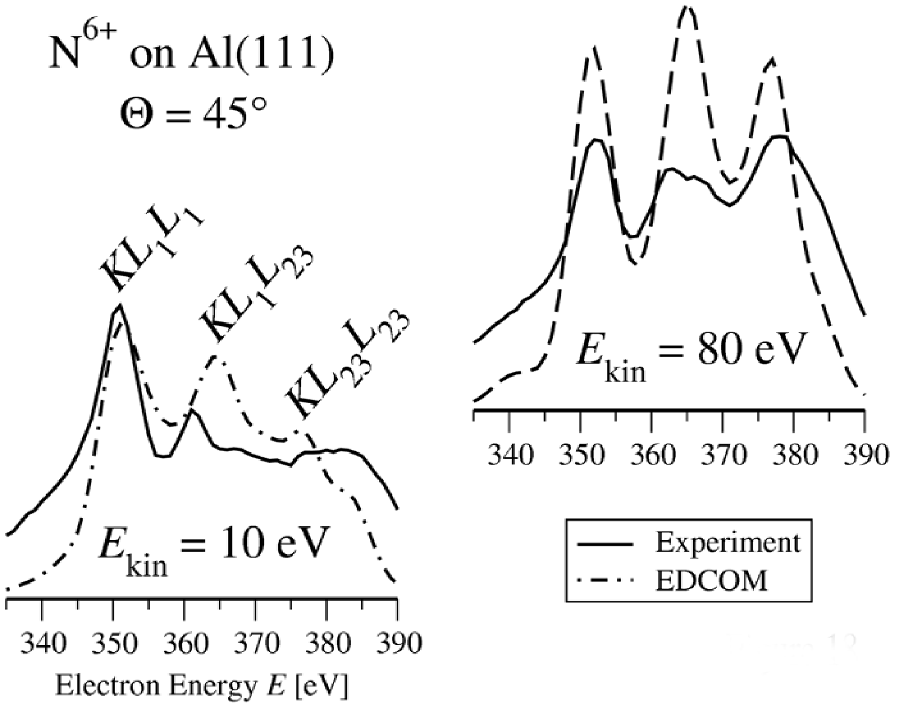

Figure 4.18. KLL spectra of N^{6+} incident under $\Theta = 45°$ on an Al(111) surface. Experimental and simulated spectra for the incident energies $E_{kin} = 10$ eV and 80 eV.

3.4.3 K-Auger spectra.

K-Auger spectra for H-like and $(1s2s)$-metastable He-like incident ions can be subdivided into a well-structured KLL region, a broad, less intense peak consisting of KLM and KLC transitions and small contributions from KXY transitions with $X, Y \in \{M, N, \ldots\}$. Fig. 4.18 shows measured and simulated KLL electron spectra for N^{6+} colliding with an Al(111) surface under $\Theta = 45°$ with $E_{kin} = 80$ eV (upper right part) and $E_{kin} = 10$ eV (lower left part). For both projectile energies, the KLL region extends between the KL_1L_1 peak at $E = 352$ eV and the $KL_{23}L_{23}$ peak at $E = 378$ eV. The peak widths reflect the spread in initial L-shell populations at the time of K-Auger decay. The broad KLM/KLC peak is situated on the high-energy side of the KLL region.

In general, the KLL sub-peak intensities sensitively depend on the ratio between the L-shell filling rate $\Gamma_L^{fill} = \Gamma_{n,L}^{AI} + \Gamma_L^{SF}$ (eqs. (4.4) and (4.11)) and KLL decay rates Γ_K^{AI}. Only crude estimates for Γ_n^{fill} are available in the relevant interaction region, and Γ_K^{AI} is known only for free ions [86, 87] (cf. section 4.3.2.1). For shells $n > 2$, we have neglected the fine-structure in our simulation.

With respect to intensity ratios between different KLL sub-peaks, the extended COM follows the experimental trend: towards increasing E_{kin}, the KL_1L_1 peak loses intensity, which is transferred into the upper part of the KLL spectrum. This can be understood in view of stronger side feeding into the $2p$-orbital when the vertex of the trajectory moves closer to the first lattice layer as E_{kin} increases [17]. Near the vertex, the projectile is very slow and the exponentially decaying SF rates in eq. (4.11) reach their maximum amplitude.

The upper edge of the experimental $KL_{23}L_{23}$ peak is situated at a higher energy than in the simulation. In order to establish such a KLL energy, all six neutralizing electrons have to be present in the L-shell. This might indicate that the SF rate Γ_n^{SF} in eq. (4.11), which yields an average L-shell population $a_L = 4.6$ at the time of K-Auger decay for $E_{kin} = 80$ eV, might be slightly underestimated.

4. Summary

This chapter reviewed some of the ideas that are currently used to model the interaction of slow, highly charged projectiles with gaseous C_{60} and metal surfaces. It has put together several applications of the (extended) dynamical COM to observables that recently have been measured in collisions with HCI. Due to the complexity of the collision system and the inherent many–electron processes, *ab-initio* calculations, based on quantum mechanical matrix elements, are currently out of reach.

For soft collisions with C_{60} targets, we discussed the formation and decay of hollow projectile ions within the dynamical COM, supplemented by a simple downstream relaxation scheme. This scheme allows for the simulation of energy differential and total yields of post–collisionally emitted projectile Auger electrons and photons. The close agreement between the dynamical COM and various measured quantities confirms the picture of large-impact-parameter capture from C_{60} as an over-barrier process, very similar to corresponding processes in both ion-atom and ion-surface collisions.

For collisions of slow multiply-charged ions with solid surfaces, the dynamical COM needed to be extended to take into account interactions at small ion–surface distances, such as electron peel–off, side feeding, and continuum promotion. We calculated the population dynamics of the projectile by Monte-Carlo sampling along the entire ion trajectory over a large number of trajectories. For the classical motion of the projectile we included all relevant binary interaction potentials between the projectile and individual surface atoms. Our results are in reasonable agreement with various experimental observables for different combinations of projectiles, target types, incident angles and beam energies. This has been achieved *without* adapting the free parameters involved in the simulation to a particular collision system.

Future investigations, both experimental and theoretical, are necessary to refine these simulations in order to better understand the exciting life of a hollow ion during and after its interaction with complex targets, such as fullerenes and surfaces.

Acknowledgments

This work was supported by the Division of Chemical Sciences, Geosciences, and Biosciences, Office of Basic Energy Sciences, Office of Science, U.S. Department of Energy. The author gratefully acknowledges stimulating discussions and fruitful collaborations with J.J. Ducrée, A. Bárány, F. Casali, H. Cederquist, C.L. Cocke, B. Fricke, L. Hägg, and B. Walch.

References

[1] M. Krämer, J. Radiat. Res. **42**, 39 (2001); M. Scholz, A.M. Kellerer, W. Kraft–Weyrather, G. Kraft, Radiat. Environ. Biophys. **36**, 59 (1997)

[2] J.D. Gillaspy, D.C. Parks, and L.P. Ratliff, J. Vac. Sci. Technol. B **16 (6)**, 3294 (1998)

[3] L.P. Ratliff, R. Minniti, A. Bard, J.D. Gillaspy, D. Parks, A.J. Black, and G.M. Whitesides, Appl. Phys. Lett **74 (4)**, 590 (1999)

[4] E. Lerner, *The Industrial Physicist*, **5 (3)**, 18 (June 1999); **5 (5)**, 18 (October 1999)

[5] D.C. Lorentz, Comments At. Mol. Phys. **33**, 125 (1997)

[6] P. Scheier, B. Dünser, R. Wörgötter, S. Matt, D. Muigg, G. Senn, and T.D. Märk, Int. Rev. in Phys. Chem. **15**, 93 (1996)

[7] D. Hathiramani, V. Schäfer, K. Aichele, U. Hartenfeller, F. Scheuermann, M. Steidl, M. Westermann, and E. Salzborn, p. 653 in *"Photonic, Electronic, and Atomic Collisions"* ed. F. Aumayr, G. Betz and H.P. Winter, World Scientific, Singapore (1998)

[8] A. Bárány, p. 641 in *"Photonic, Electronic, and Atomic Collisions"* ed. F. Aumayr, G. Betz and H.P. Winter, World Scientific, Singapore (1998)

[9] H. Shen, P. Hvelplund, D. Mathur, A. Bárány, H. Cederquist, N. Selberg, and D.C. Lorentz, Phys. Rev. A **52**, 3847 (1995)

[10] H.G. Busmann, Th. Lill, B. Reif, and I.V. Hertel, Surf. Sci. **272**, 146 (1992)

[11] J. Jin, H. Khemliche, M.H. Prior, Z. Xie, Phys. Rev. A **53**, 615 (1996)

[12] B. Walch, U. Thumm, M. Stöckli, C.L. Cocke, and S. Klawikowski, Phys. Rev. A **58**, 1261 (1998)

[13] J.P. Briand, L. de Billy, J. Jin, H. Khemliche, M.H. Prior, Z. Xie, M. Nectoux, and D. Schneider, Phys. Rev. A **53**, R2925 (1996)

[14] U. Thumm, Phys. Rev. A **55**, 479 (1997)

[15] S. Martin, J. Bernard, L. Chen, A. Denis, and J. Désesquelles, Eur. Phys. J. D **4**, 1 (1998)

[16] B. Walch , C.L. Cocke, R. Voelpel, and E. Salzborn, Phys. Rev. Lett. **72**, 1439 (1994)

[17] J. Thomaschewski, J. Bleck-Neuhaus, M. Grether, A. Spieler, and N. Stolterfoht, Phys. Rev. A**57**, 3665 (1998)

[18] M. Schulz, C.L. Cocke, S. Hagmann, and M. Stöckli, Phys. Rev. A **44**, 1653 (1991)

[19] S. Winecki, C.L. Cocke, D. Fry, and M.P. Stöckli, Phys. Rev. A **53**, 4228 (1996)

[20] J. Burgdörfer, P. Lerner, and F.W. Meyer, Phys. Rev. A **44**, 5674 (1991)

[21] J. Burgdörfer, p. 517 in *Review of Fundamental Processes and Applications of Atoms and Ions*, ed. C. D. Lin, World Scientific, Singapore, (1993)

[22] J. Burgdörfer, C. Reinhold, and F.W. Meyer, Nucl.Instrum.Methods Phys. Res. B **98**, 415 (1995)

[23] M.W. Clark, D. Schneider, D. Dewitt, J.W. McDonald, R. Bruch, U.I. Safranova, I.Y. Tolstikhina, and R. Schuch, Phys. Rev. A **47**, 3983 (1993)

[24] J.P. Briand, B. d'Etat-Ban, D. Schneider, M.A. Briere, V. Decaux, J.W. McDonald, and S. Bardin, Phys. Rev. A**53**, 2194 (1996)

[25] F.W. Meyer, C.C. Havener, and P.A. Zeijlmans van Emmichoven, Phys. Rev. A **48**, 4476 (1993)

[26] H. Kurz, F. Aumayr, HP. Winter, D. Schneider, M.A. Briere, and J.W. McDonald, Phys. Rev. A **49**, 4693 (1994)

[27] A. Bárány and C.J. Setterlind, Nucl.Instrum.Methods Phys. Res. B **98**, 407 (1995)

[28] A.G. Borisov, R. Zimny, D. Teillet–Billy, and J.P. Gauyacq, Phys. Rev. A **53**, 2457 (1996)

[29] J. Limburg, S. Schippers, I. Hughes, R. Hoekstra, R. Morgenstern, S. Hustedt, N. Hatke, and W. Heiland, Phys. Rev. A. **51**, 3873 (1995)

[30] W. Huang, H. Lebius, R. Schuch, M. Grether, and N. Stolterfoht, Phys. Rev. A**56**, 3777 (1997)

[31] U. Thumm, J.Ducreé, P. Kürpick, and U. Wille, Nuc. Instrum. Methods Phys. Res. B**157**, 11 (1999); B. Bahrim, P. Kürpick, U. Thumm and U. Wille, ibid **164–165**, 614 (2000)

[32] Q. Yan, D.M. Zehner, and F.W. Meyer, Phys. Rev. A **54**, 641 (1996)

[33] C. Auth, and H. Winter, Phys. Lett. A **217**, 119 (1996)

[34] J. Limburg, S. Schippers, R. Hoekstra, R. Morgenstern, H. Kurz, F. Aumayr, and HP. Winter, Phys. Rev. Lett. **75**, 217 (1995)

[35] F. Aumayr, p. 631 in *Proceedings of the XIX'th Int. Conf. on the Physics of Electronic and Atomic Collisions*, ed. L. Dubé et al., AIP Conf. Proc. 360, AIP press, New York (1995)

[36] L. Hägg, C.O. Reinhold, and J. Burgdörfer, Phys. Rev. A**55**, 2097 (1997); Nucl.Instrum.Methods Phys. Res. B **125**, 133 (1997)

[37] J.P. Briand, S. Thuriez, G. Giardino, G. Borsoni, V. Le Roux, M. Froment, M. Eddrief, C. de Villeneuve, B. d'Etat-Ban, and C. Sébenne, Phys. Rev. A **55**, R2523 (1997)

[38] J.J. Ducrée, F. Casali, and U. Thumm, Phys. Rev. A**57**, 338 (1998)

[39] H. Winter, Europhys. Lett. **18** 207 (1992); J. Phys.: Condens. Matter **8**, 10149 (1996)

[40] J.J. Ducrée, J. Mrogenda, E. Reckels, M. Rüther, A. Heinen, Ch. Vitt, M. Venier, J. Leuker, H.J. Andrä, and R. Díez Muiño, Phys. Rev. A**57**, 1925 (1998)

[41] H. Ryufuku, K. Sasaki and T. Watanabe, Phys. Rev. A**21**, 745 (1980)

[42] A. Niehaus, J. Phys. B**19**, 2925 (1986)

[43] A. Bárány, p. 246 in *Proceedings of the XVI Int. Conf. on the Physics of Electronic and Atomic Collisions*, ed. Dalgarno et al, AIP Conf. Proc. 205, AIP, New York, (1990)

[44] U. Thumm, J. Phys. B **27**, 3515 (1994) In this reference, a factor 1/2 is not printed in the self-image potentials. This factor, however, was included in all computations. In addition, the present work uses a different sign convention in the definition of interaction potentials.

[45] U. Thumm, J. Phys. B **28**, 91 (1995)

[46] U. Thumm, T. Baştuğ, and B. Fricke, Phys. Rev. A **52**, 2955 (1995)

[47] R. D. Cowan, *The Theory of Atomic Structure and Spectra*, University of California Press, Berkeley, (1981)

[48] J.J. Ducrée, H.J. Andrä, and U. Thumm, Phys. Rev. A**60**, 3029 (1999)

[49] M.J. Puska and R.M. Nieminen, Phys. Rev. A**47**, 1181 (1993)

[50] J.L Martins, N. Troullier, and J.H. Weaver, Chem. Phys. Lett. **180**, 457 (1991)

[51] C. Yannouleas, and U. Landman, Chem. Phys. Lett. **217**, 175 (1994)

[52] T. Baştuğ, P. Kürpick, J. Meyer, W.–D. Sepp, B. Fricke, and A. Rosen, Phys. Rev. B **55**, 5015 (1997)

[53] C. Lifshitz, M. Iraqi, T. Peres, and J.E. Fischer, Rapid Commun. Mass Spectrom. **5**, 238 (1991)

[54] I.V. Hertel, H. Steger, J. de Vries, B. Weisser, C. Menzel, B. Kamke, and W. Kamke, Phys. Rev. Lett. **68**, 784 (1992)

[55] N. Selberg, A. Bárány, C. Biedermann, C.J. Setterlind, H. Cederquist, A. Langereis, M.O. Larsson, A. Wännström, and P. Hvelplund, Phys. Rev. A **53**, 874 (1996)

[56] U. Thumm, A. Bárány, H. Cederquist, L. Hägg, and C.J. Setterlind, Phys. Rev. A **56**, 4799 (1997)

[57] P. Benoit–Cattin, A. Bordenave–Montesquieu, M. Boudjema, A. Gleizes, S. Dousson, and D. Hitz, J. Phys. B **21**, 3387, (1988)

[58] R. Ali, C.L. Cocke, M.L.A. Raphaelian, and M. Stöckli, J. Phys. B **26**, L117, (1993); Phys. Rev. A **49**, 3586 (1994)

[59] N. Vaeck and J.E. Hansen, J. Phys. B **28**, 3523, (1995), and refs. therein.

[60] K.R. Karim, S.R. Grabbe, and C.P. Bhalla, J. Phys. B **29**, 4007 (1996)

[61] Z. Chen and C.D. Lin, J. Phys. B **26**, 957, (1993)

[62] H. Cederquist, private communication.

[63] P. Sakurai, *M.Sc. Thesis, Univ. Stockholm*, unpublished (1997)

[64] D. S. Gemmell, Rev. Mod. Phys. **46**, 129 (1974)

[65] C. Lemell, H. P. Winter, F. Aumayr, J. Burgdörfer, and F. Meyer, Phys. Rev. A **53**, 880 (1996)

[66] J. Burgdörfer, C. Reinhold, L. Hägg, and F. Meyer, Aust. J. Phys. **49**, 527 (1996)

[67] H. Winter, J. Phys: Condens. Matter **8**, 10149 (1996)

[68] J. Burgdörfer and F. Meyer, Phys. Rev. A **47**, R20 (1993)

[69] H. Winter, C. Auth, R. Schuch, and E. Beebe, Phys. Rev. Lett. **71**, 1939 (1993)

[70] R. Díez Muiño, N. Stolterfoht, A. Arnau, A. Salin, and P. M. Echenique, Phys. Rev. Lett. **76**, 4636 (1996)

[71] L. Folkerts and R. Morgenstern, Europhys. Lett. **13**, 377 (1990)

[72] N. Stolterfoht, R. Köhrbrück, M. Grether, A. Spieler, A. Arnau, R. Page, A. Saal, J. Thomaschewski, and J. Bleck-Neuhaus, Nucl. Instrum. Methods Phys. Res., Sect. B **99**, 4 (1995)

[73] C. Lemell, H. P. Winter, F. Aumayr, J. Burgdörfer, and C. Reinhold, Nucl. Instrum. Methods Phys. Res., Sect. B **102**, 33 (1995)

[74] F. W. Meyer, L. Folkerts, H. O. Folkerts, and S. Schippers, Nucl. Instrum. Methods Phys. Res., Sect. B **98**, 441 (1995)

[75] L. Folkerts, S. Schippers, D. M. Zehner, and F. W. Meyer, Phys. Rev. Lett. **74**, 2204 (1995), erratum: Phys. Rev. Lett. **75**, 983 (1995)

[76] S. Winecki, M. P. Stöckli, and C. L. Cocke, Phys. Rev. A **56**, 538 (1997)

[77] R. Díez Muiño, A. Arnau, and P. M. Echenique, Nucl. Instrum. Methods Phys. Res., Sect. B **98**, 420 (1995)

[78] M. Grether, A. Spieler, R. Köhrbrück, and N. Stolterfoht, Phys. Rev. A **52**, 426 (1995)

[79] R. Díez Muiño, A. Salin, N. Stolterfoht, A. Arnau, and P. M. Echenique, Phys. Rev. A **57**, 1126 (1998)

[80] S. Winecki, M. P. Stöckli, and C. L. Cocke, Phys. Rev. A **55**, 4310 (1997)

[81] D. Niemann, M. Grether, A. Spieler, N. Stolterfoht, C. Lemell, F. Aumayr, and H. P. Winter, Phys. Rev. A **56**, 4774 (1997)

[82] J. Limburg, J. Das, S. Schippers, R. Hoekstra, and R. Morgenstern, Phys. Rev. Lett. **73**, 786 (1994)

[83] P. Kürpick, U. Thumm, and U. Wille, Nucl. Instrum. Methods Phys. Res., Sect. B **125**, 273 (1997)

[84] P. Kürpick and U. Thumm, Phys. Rev. A **58**, 2174 (1998); U. Thumm, *Book of invited papers, XXII Internat. Conf. on the Physics of Photonic, Electronic, and Atomic Collisons*, Santa Fe, NM, ed. S. Datz et. al. (Rinton Press, 2002) p. 592

[85] H. Eder, M. Vana, F. Aumayr, H. P. Winter, J. I. Juaristi, and A. Arnau, Physica Scripta **T 73**, 322 (1997)

[86] J. Hansen, O. Schraa, and N. Vaeck, Physica Scripta **T41**, 41 (1992)

[87] S. Schippers, J. Limburg, J. Das, R. Hoekstra, and R. Morgenstern, Phys. Rev. A **50**, 540 (1994)

II

INTERACTIONS WITH GASEOUS TARGETS